A Temperature Sensor for Measuring Dielectric Loss Heating in a Dielectrophoresis Device

Imtiaz Hossen
Marquette University

A TEMPERATURE SENSOR FOR MEASURING DIELECTRIC LOSS HEATING IN A DIELECTROPHORESIS DEVICE

by

Imtiaz Hossen

A Thesis submitted to the Faculty of the Graduate School,
Marquette University,
in Partial Fulfillment of the Requirements for
the Degree of Master of Science

Milwaukee, Wisconsin

August 2020

ABSTRACT
A TEMPERATURE SENSOR FOR MEASURING
DIELECTRIC LOSS HEATING
IN A DIELECTROPHORESIS DEVICE

Imtiaz Hossen

Marquette University, 2020

Dielectrophoresis is an extensively used technique in the field of biomedical science that manipulates particles in a non-uniform electric field. One of its drawbacks is heat dissipation during the DEP operation that raises the local temperature of the DEP device. Temperature increases during dielectrophoresis (DEP) can affect the response of biological entities and ignoring the effect can mislead the result of the analysis. The heating mechanism of a DEP device is typically considered to be the result of Joule heating as bare electrodes are used in a conductive solution. However, when electrodes are insulated from the solution the presence of heat is overlooked without appropriate analysis.

The measurement of the local temperature of a microdevice is a complex task. A temperature increase between interdigitated electrodes (IDEs) in presence of DI solution has been measured with an integrated micro temperature sensor between IDEs to be as high as 9 °C at 1.5 MHz with a 26 Vpp applied voltage to our ultra-low thermal mass DEP device. Our experiment and analysis indicate that the heating mechanism in insulated DEP electrodes is due to the dielectric loss (Debye relaxation). The analytical result of the power dissipation due to the dielectric loss is in good agreement with the experiment data.

ACKNOWLEDGMENTS

Imtiaz Hossen

At first, I would like to express my sincere gratitude to my thesis supervisor Dr. Chung Hoon Lee for his continuous support of my MS study and research. His patience, motivation, and guidance helped me a lot in my journey. He continuously enabled me to guide me in the right direction whenever I needed it.

I want to thank Dr. James Richie and Dr. Henry Medeiros for their time and valuable comments on this thesis. I would also like to thank the current member of the Nanoscale Device Laboratory, Avijit Hira for his support and assistance.

I am grateful for this opportunity provided by Marquette University, Department of Electrical and Computer Engineering.

DEDICATION

I would like to dedicate this work to my ever-supporting family and friends.

Thank You

TABLE OF CONTENTS

LIST OF TABLES

LIST OF FIGURES

CHAPTER 1

INTRODUCTION

1.1 The importance of measuring temperature

Temperature is one of the most measured parameters because of its importance in everyday life [1]. In a home, people control the room temperature by using a heater and air-conditioner in different seasons. It is necessary to monitor the temperature to know how much the room should be heated or cooled or what clothing people should wear. Refrigerator and cold storage are used for storing different foods such as vegetables, dairy products, meats, etc. Storing food at a certain temperature can prevent it from spoiling. Monitoring the temperature continuously in such appliances is necessary for controlling the desired temperature. Even for serving warm foods, it is necessary to monitor the temperature. Many harmful pathogens can be reduced or eliminated at a certain temperature [2]. In industrial production, such as metal processing and plastic production, temperature monitoring is one of the most important tasks to control quality and safety and to increase the production rate. In most industrial applications, accurate temperature measurement is crucial. Inaccurate temperature measurement can be harmful to process efficiency, energy consumption, product quality, and process safety [1]. Even a small measurement error can cause huge losses for some industries. Inaccurate temperature measurement in pharmaceutical processing can ruin a batch of products that can cost hundreds of thousand dollars [1]. In chemical reactions, the exothermic process can lead to explosions if the temperature is not monitored continuously and accurately [1].

Body temperature measurement is important for medical care. The human body can maintain its temperature within a safe range. When body temperature falls or rises beyond this safe range, we feel sicknesses such as fever, hypothermia [3], heatstroke. These sicknesses can be identified by measuring body temperature using a thermometer. More recently, researchers are trying to kill cancer cells by elevating body temperature to $39°C$-$40°C$ [3]. In such a case, precise measurement of temperature is necessary to ensure no damage to normal cells. Many researchers are interested in measuring single-cell temperature [4]. The temperature of a cell changes due to metabolic processes or biochemical reactions [4]. Measuring single-cell temperature will provide new physiological information to understand cellular activities.

Temperature sensors are most common among all the sensing technologies [5]. Different sensing technologies such as pressure, force, position, level, and flow need to know the actual or relative temperature for accurate measurement [5]. Pressure sensors usually measure with Wheatstone bridge configurations. Temperature changes the resistances of the Wheatstone bridge. Without knowing the temperature and correcting the measured output, the result is useless.

1.2 Different temperature measurement devices

Measurement of temperature needs a sensor to detect the temperature variation, a signal conditioning circuit to amplify the low output level of the sensor, and a display system. The combination of all these components is called a temperature measurement system [1]. There are different types of temperature measuring devices that are suitable for specific applications. It is a complicated task for inexperienced engineers to select a suitable temperature measurement system for a particular application. Choosing a temperature measurement device

depends on many factors, such as range, sensitivity, repeatability, accuracy, and cost [1]. Accuracy is the closeness of measured temperature to actual temperature. Repeatability is a measure, showing the same temperature in repeated measurements for an unchanged environment. Sensitivity is the lowest temperature that can be detected in a sensor system. Temperature sensors can be classified into two types [6]:

- Contact temperature sensor
- Non-contact temperature sensor

The contact type sensor requires physical contact with the object to measure its temperature. The sensor uses heat that transfers from the object to the sensor by conduction. The non-contact type sensor uses convectional heat and radiated heat to measure the temperature change [6]. These two types can also be sub-classified into two classes: mechanical and electrical temperature sensors. All these types are discussed below.

1.2.1 Glass thermometer

This type of thermometer is commonly used for measuring the weather and body temperature. This instrument consists of a glass tube with a small diameter bore connected to a reservoir called a bulb [7]. The bulb contains a special liquid. The glass tube is shaped in a way that acts as a lens to broaden the apparent width of the liquid column [7]. This liquid expands or contracts in response to any change in temperature. The thermal expansion of the liquid is larger than the solid. When the temperature rises, the liquid in the bulb expands more than the glass tube and liquid height increases in the bore of the glass tube [7]. A marked scale on the tube and the position of liquid indicates the temperature. Construction of a simple glass thermometer and its cross-section is shown in Fig. 1.1 .

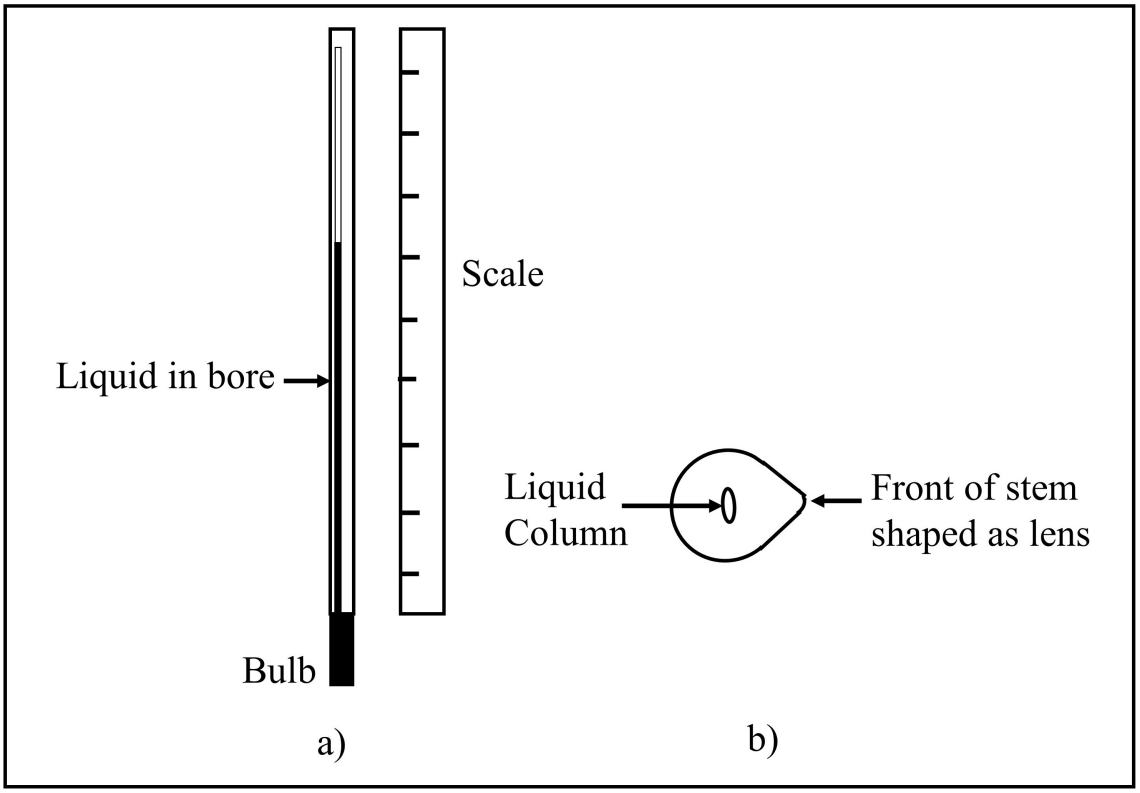

Figure 1.1: A simple glass thermometer, a) Construction of a thermometer, b) Cross-sectional view. Graph reproduced from [7]

Earlier glass tubes used mercury as a working liquid. Nowadays, liquids such as alcohol, toluene, pentane are used instead of mercury because of mercury's hazardous impact on the environment [8]. The temperature ranges of different liquids are given below in Table 1.1.

The accuracy of glass thermometers depends on the actual devices, and the range of accuracy is $0.01°C$ to $4°C$ [10]. Non-uniformity in bore leads to different inaccuracies in different devices. Sometimes a device can be accurate at calibration points but inaccurate at intermediate points [10].

Liquid	Temperature range($^{\circ}C$)
Mercury	-35 to 510
Alcohol	-80 to 70
Pentane	-200 to 30
Toluene	-80 to 100
Creosote	-5 to 200

Table 1.1: Temperature ranges of glass thermometer for different liquids [9].

1.2.2 Thermocouple

The thermocouple is a temperature sensor that consists of two dissimilar metal wires fused to form two junctions of dissimilar metal [11]. One junction is kept at a cool temperature called the reference junction, and another junction at hot temperature is the measuring junction. The operating principle of the thermocouple is simple. When two junctions are kept at two different temperatures because of the thermo-electric or Seeback effect, a constant voltage difference is produced [10]. The simple construction of a thermocouple is represented in Fig. 1.2. This voltage difference is proportional to the temperature difference between two junctions. If two junctions are at the same temperature or if two similar metals are used to make the junctions, the output voltage will be zero. The output voltage of the thermocouple is in the millivolt range, so amplification is required [11]. Thermocouples are low-cost devices that can operate at a very high-temperature range and can measure very high temperatures. As temperature increases, the voltage will increase until it reaches the maximum voltage, which limits the maximum measurable temperature. For different metal pairs, the measurable temperature limits are different. Table 1.2 shows different metal pairs and their detection ranges. Type J, type K, and type T metal pairs are commonly used for general temperature measurement. For many

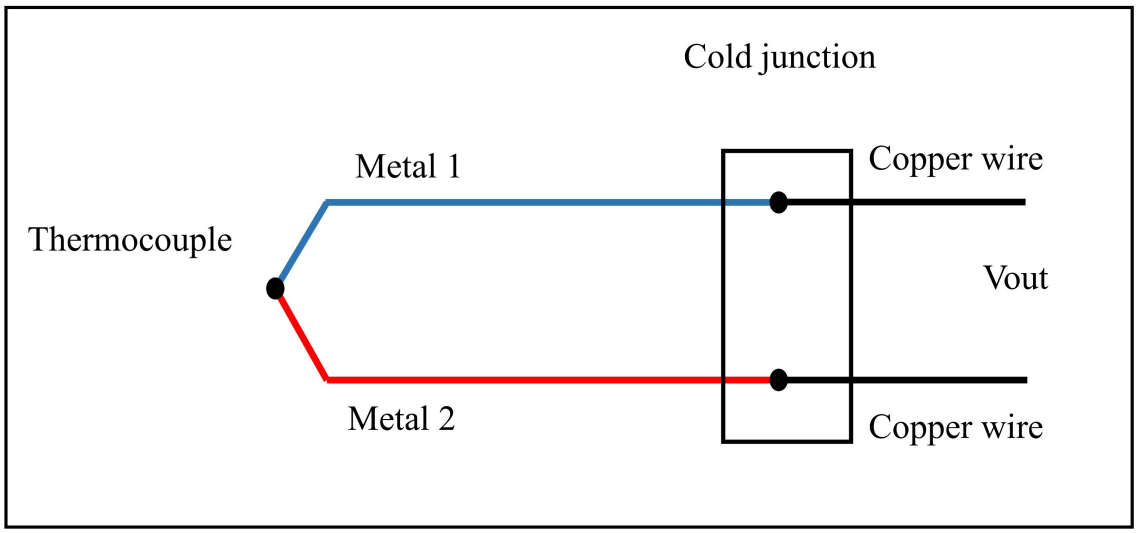

Figure 1.2: A schematic diagram of thermocouple. Graph reproduced from [5]

Code type	Conductors	Range($^\circ C$)
E	Chromel / Constantan	-268 to 800
J	Iron / Constantan	-196 to 700
K	Chromel / Alumel	-250 to 1100
N	Nicrosil / Nisil	0 to 1250
T	Copper / Constantan	-226 to 850

Table 1.2: Temperature ranges of different pairs of thermocouples [10].

applications, thermocouple wire needs to be isolated electrically or chemically from the environment. Different insulation materials are used to isolate the thermocouples from the environment, such as PVC for $150^\circ C - 230^\circ C$, Teflon for $1250^\circ C - 2273^\circ C$, glass fiber for $250^\circ C - 400^\circ C$, and polyimide for $400^\circ C - 2269^\circ C$ [10]. To support and electrically isolate the thermocouple, a metal sheath is used that can protect to $1250^\circ C$ [10]. Ceramic sheaths can protect thermocouple even at high temperatures [10]. The output voltage-temperature relationship of thermocouple is reasonably linear [11]. Fig. 1.3 shows the relation

between output voltage and temperature.

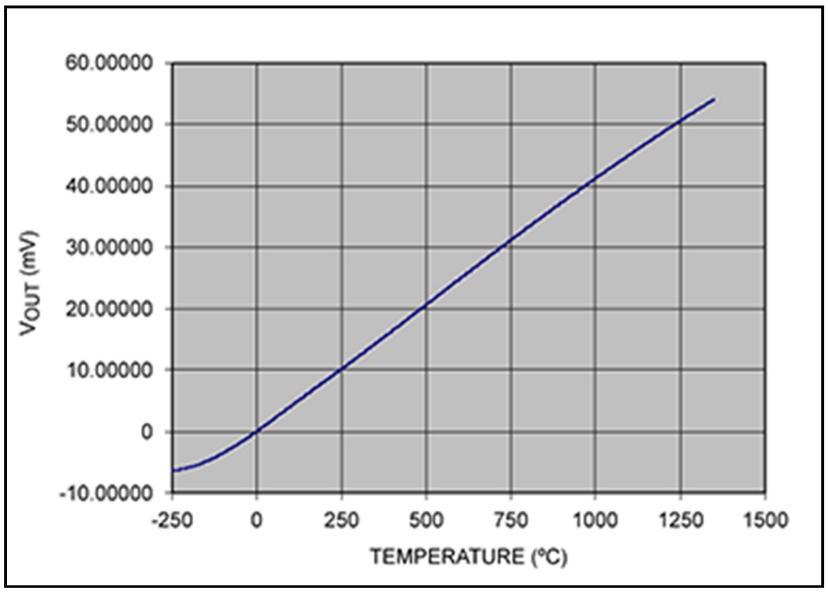

Figure 1.3: Thermocouple output voltage vs. temperature relation [11].

The response speed of thermocouples is fast enough to measure temperature continuously. The disadvantages of thermocouples are low sensitivity, very low output voltage at low temperature, noise prone and lower accuracy than resistor temperature detectors [10].

1.2.3 Thermistor

Thermistors are resistors that change their resistance as temperature changes. Thermistor sensors are used in applications where accuracy is a high priority [5]. Thermistors are made from conductive materials such as ceramic and polymer [11]. The temperature range is about $150^{\circ}C$, which is a very low range compared to a thermocouple [11]. There are two types of thermistors,

- Negative Temperature Coefficient (NTC)
- Positive Temperature Coefficient (PTC)

NTC thermistors are used in most applications [11]. In NTC, the resistance increases as the temperature decreases. Thermistors are passive devices that need an excitation current to produce a measurable voltage. Its relationship with temperature is very nonlinear, so the measurement of temperature is more complex than the resistor temperature detector (RTD). A typical NTC thermistor's resistance-temperature relation is given in Fig. 1.4.

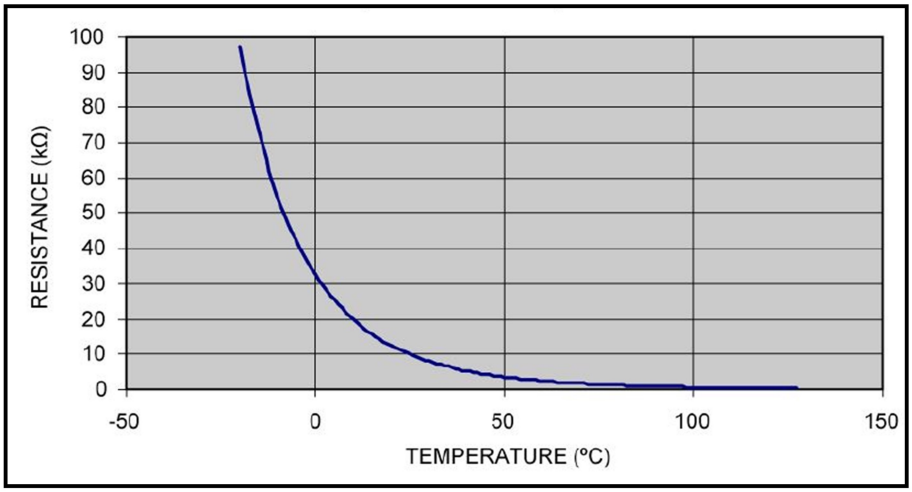

Figure 1.4: Thermistor resistance vs. temperature relation [11]

The Steinhart-Hart equation is used for interpolation of temperature as a function of thermistor resistance [12].

$$1/T = A + BlogR + C(logR)^3 \tag{1.1}$$

where R is the thermistor resistance, T is the temperature in Kelvin, and A, B, C are curve-fitting constants determined through a calibration process for a given thermistor material. Thermistor sensors are used in applications where accuracy is a high priority.

Common circuitry for temperature measurement using a thermistor is shown in Fig. 1.5.

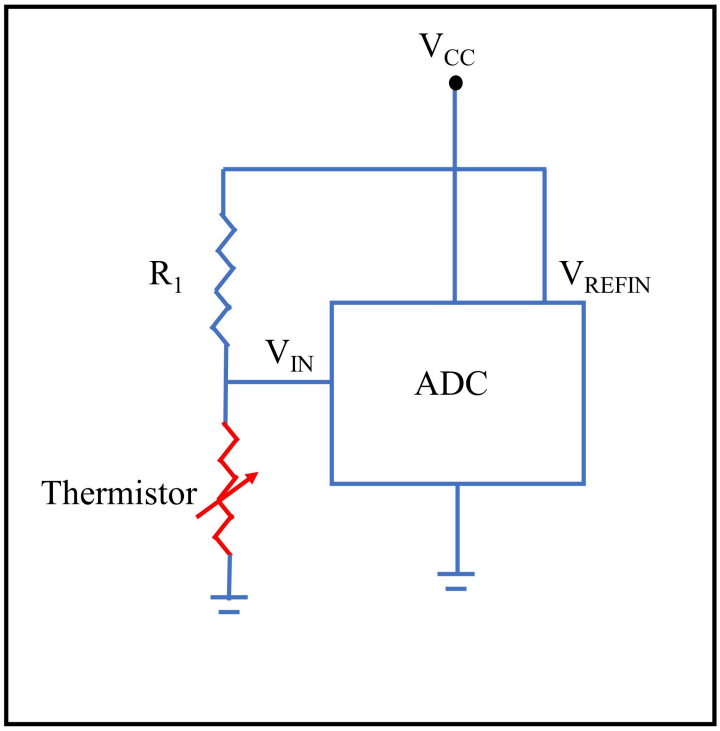

Figure 1.5: A schematic diagram of thermistor circuitry [11].

The thermistor and a fixed resistor form a voltage divider circuit. The output of the thermistor is connected to an analog to digital converter (ADC) for digitization.

1.2.4 Resistor temperature detector (RTD)

Like thermistors, RTD sensors also use the property of resistance-temperature dependency. Their main difference is the material used to form the devices. Unlike a thermistor, a RTD is made from pure metal such as platinum, nickel or copper. They have a positive temperature coefficient (PTC).

The temperature-resistance relation is almost linear, which allows for accurate temperature measurement. The temperature-resistance relation is described by the Callendar-Van Dusen equation:

$$R(T) = R_0(1 + aT + bT^2 + c(T - 100)T^3) \tag{1.2}$$

where, T = temperature ($^\circ C$), R(T) = resistance at T$^\circ C$ and R_0 = resistance at T = $0^\circ C$. Their sensitivity is low compared to the thermistor. The resistance change in response to temperature change is very low in RTD sensors [5]. However, RTD sensor response in temperature is more linear than thermistor. Fig. 1.6 shows the temperature vs. resistance ratio of both platinum RTD (Pt-100) and thermistors.

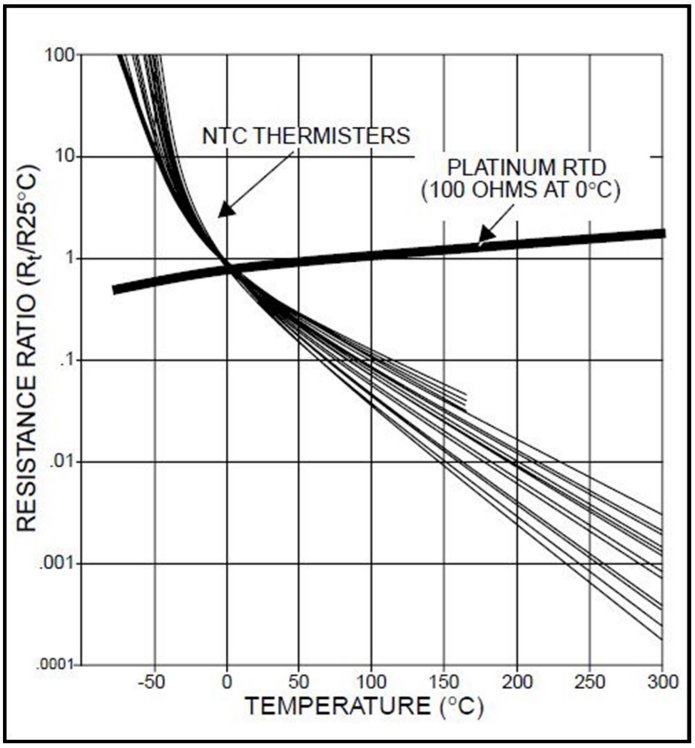

Figure 1.6: Temperature vs. resistance ratio of platinum RTD and thermistor sensors [5].

In Fig. 1.6, RTD has a positive temperature coefficient, and the thermistor has a negative temperature coefficient. The temperature coefficient of RTD is very low compared to the thermistor. So the thermistor is more accurate than RTD. There are three different types of RTD [13]:

- Wire wound RTD
- Coiled element RTD
- Thin-film RTD

The microfabricated thin-film RTD is very popular because of its high sensitivity and fast thermal response [13]. The easy fabrication of RTD and revolutionary improvement of MEMS technologies increase the opportunities to use this sensor for researches. Platinum RTDs are the most common and accurate RTD [11]. In the market, they are available with 100 Ω and 1000 Ω resistances called PT-100 and PT-1000. The temperature coefficient of PT-100 is .00375 $\Omega/^{\circ}C$ [11]. The temperature range for Platinum RTD is about $-200^{\circ}C$ to $850^{\circ}C$ [7].
RTDs are also passive sensors. They need an excitation current and then the resistance is measured by monitoring the voltage across the sensor. There are 3 types of RTD configurations,

- Two-wire configuration
- Three-wire configuration
- Four-wire configuration

Depending on the application, RTD sensors are connected in one of these configurations. Among them, the two-wire configuration is the simplest. In Fig. 1.7, R_b is the RTD sensor. The measured resistance in this configuration is $R_t = R_1 + R_2 + R_b$. The two-wire configuration is the least accurate as it has no way to eliminate the lead wire resistance. This configuration is generally adopted

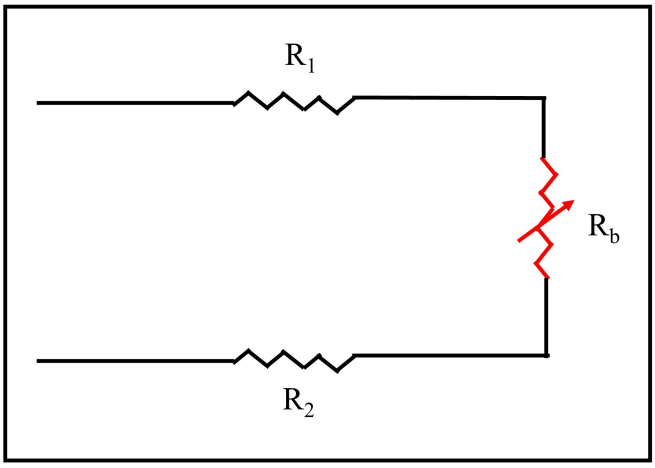

Figure 1.7: Two wire configuration

when the resistance of the lead wire is very small, and precision is not so important.

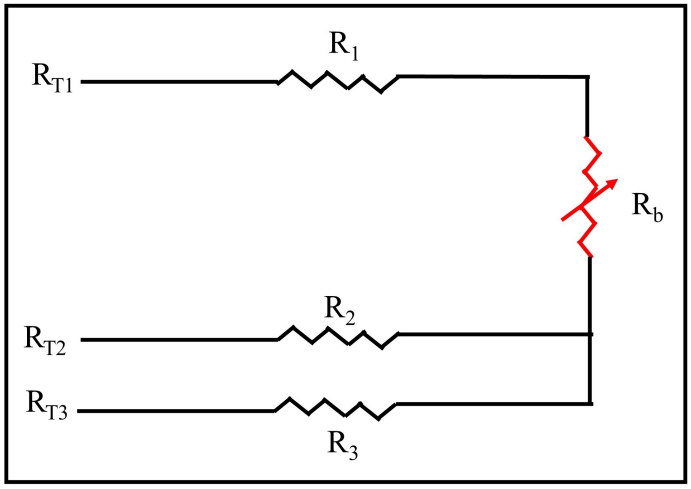

Figure 1.8: Three wire configuration

In the three-wire configuration, an extra wire carries excitation current to eliminate the effect of wire resistance, but wire resistances must be equal. In Fig. 1.8, resistance is measured by subtracting resistance between terminal R_{T1},

R_{T2} and between terminal R_{T2}, R_{T3}.

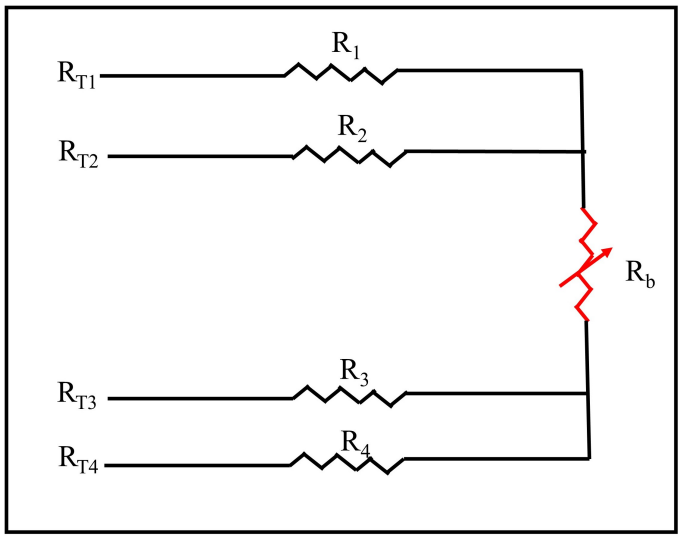

Figure 1.9: Four wire configuration

Four-wire Kelvin measurement is a precise measurement configuration that is used when lead wires are very long. In Fig. 1.9 , current is applied between terminals R_{T1} and R_{T4}, and voltage is sensed between terminals R_{T2} and R_{T3}. This configuration eliminates the effect of lead wire resistance. For the four-wire configuration, the same resistance in all lead wires is not required.

1.2.5 Fiber optic temperature sensor

In different applications, it is essential to measure temperature using a non-electrical method. Such temperature measurement sensors have many advantages particularly in explosive hazard locations and areas with strong electric or magnetic fields [14]. The fiber optic temperature sensors are unaffected by electromagnetic interference and do not carry electrical current [14]. There are some requirements for using such a sensor in different applications. The most

important requirement is the sensor must detect only the temperature-dependent change of an optical signal, therefore it is needed to isolate it from the other changes of source intensity, the optical connector loss, and the transmission loss of fibers [15].

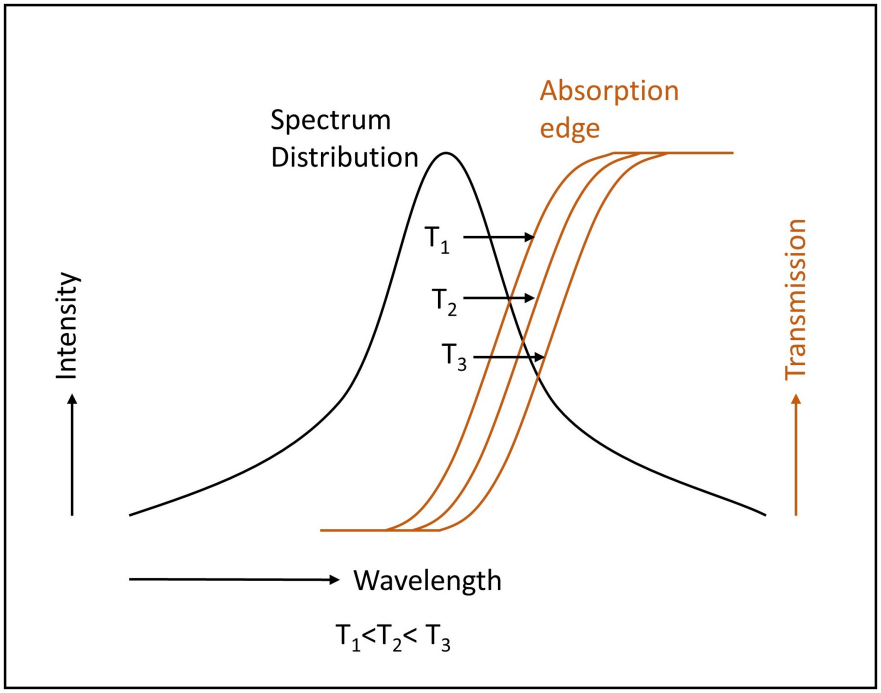

Figure 1.10: Basic principle of temperature sensing system. Graph reproduced from [15].

The principle of the sensing system is shown in Fig. 1.10. The energy gap of most semiconductors decreases almost linearly with increasing the temperature T near the room temperature [15]. Therefore, the wavelength of fundamental optical absorption edge shifts towards longer wavelength with T. When a LED with a radiation spectrum coincident with a selected semiconductor, the intensity of the transmitted light decreases with T [15]. Fig. 1.11 shows the schematic configuration of a typical fiber optic temperature measurement system.

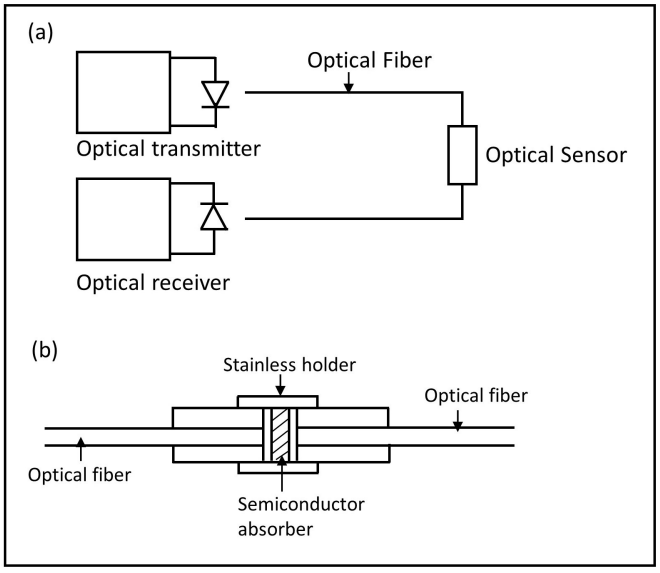

Figure 1.11: (a) Schematic diagram of the fiber-optic measurement instrument for temperature (b) Configuration of the fiber-optic temperature sensor. Graph reproduced from [15].

In Fig. 1.11.b, a thin layer of semiconductor chip sandwiched between two ends of fibers inside of a stainless holder. The incoming optical fiber guides the light from the source (LED) to the detector (avalanche photodiode). When light transmitted through the semiconductor chip, the intensity is modulated by the temperature [15]. The transmitted light is received by the outgoing optical fiber and guided to a photodetector. The temperature is monitored by measuring the output voltage of the detector.

The fiber optic temperature is easy to manufacture at a low cost [15]. The accuracy of this sensor is about $1°C$ and the temperature range is $-10°C$ to $300°C$ [15].

1.2.6 Forward looking infrared camera

A thermal imaging camera is a compact system that looks just like a digital video camera or digital photo camera. It is a reliable non-contact instrument that

can scan and visualize the temperature distribution of entire surfaces quickly [16]. The accuracy of the thermal imaging camera is about $\pm 5^{\circ}C$ [16].

A thermal imaging camera converts the intensity of radiation in the infrared part of the electromagnetic spectrum to a visible [16]. The primary source of infrared radiation is heat or thermal radiation. Objects that have a temperature above absolute zero ($-273.15^{\circ}C$ or 0K) emit radiation in the infrared region. The emitted radiation is a function of the temperature of the material [16].

In this system, the infrared energy from an object is focused by the optics onto an infrared detector. The detector sends the information to sensor electronics for image processing. The electronics translate the data coming from the detector into an image that can be viewed in the viewfinder or on a standard video monitor or LCD screen. Infrared thermography is the art of transforming an infrared image into a radiometric one, which allows temperature values to be read from the image [16]. So every pixel in the radiometric image is, in fact, a temperature measurement.

1.3 Dielectrophoresis and dielectric heat

Cell capture has many biomedical applications such as cancer research [17], cell detection [18], drug screening [19] and blood plasma separation [20]. Cell capture techniques can be classified into two classes [21],

- Nonelectrokinetic
- Electrokinetic

The electrokinetic method uses an electric field to influence the motion of cells. Two different phenomena occur in the electrokinetic method [21],

- Electrophoresis
- Dielectrophoresis (DEP)

In electrophoresis, the charged particle migrates due to the interaction between net charge of a particle and electric field [21]. The electric field is created by a DC voltage applied between two electrodes [21]. Fig. 1.12 represents the mechanism of the electrophoresis technique.

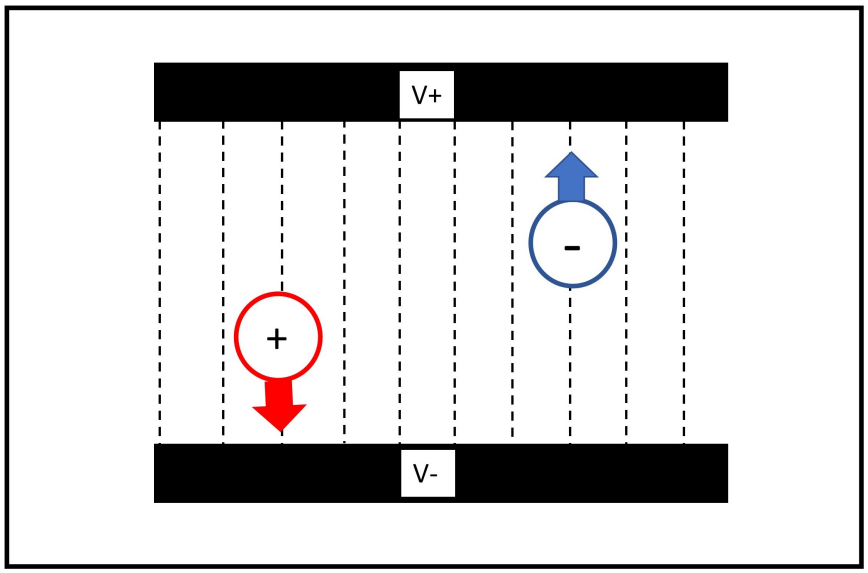

Figure 1.12: A schematic diagram of the electrophoresis mechanism [22].

Dielectrophoresis is different from electrophoresis in two ways. First, AC voltage applied in DEP rather than DC. Second, the DEP force acts on neutral particle rather than charge particle. The details of dielectrophoresis are given below.

1.3.1 Dielectrophoresis

Dielectrophoresis is one of the popular techniques used to separate, sort, transport, and manipulate cells of different sizes [23]. In this technique, the motion of neutral particles is caused by the polarization in a non-uniform electric field [23]. In dielectrophoresis, AC current is applied to electrodes to create a

non-uniform electric field; this electric field gradient interacts with the induced dipole moment of the particle [23]. The polarized charge experiences a force that can move the particle to a region of high or low electric field [23]. Particle kinetic depends on the size of electrodes, frequency of AC current, the dielectric constant of the particle, the dielectric constant of the fluid, the polarization of a particle, etc. Particles polarize under the influence of the electric field. If the particles are more polarizable than the media, particles are attracted to the increasing electric field region, this refers to positive DEP [21]. If the media is more polarizable than the particles, particles repulse from the increasing electric field region, which refers to negative DEP [21]. Fig. 1.13 shows a positive DEP effect in the red particle and a negative DEP effect in the blue particle. In Fig. 1.13, two dissimilar sizes of electrodes are used to make a non-uniform electric field.

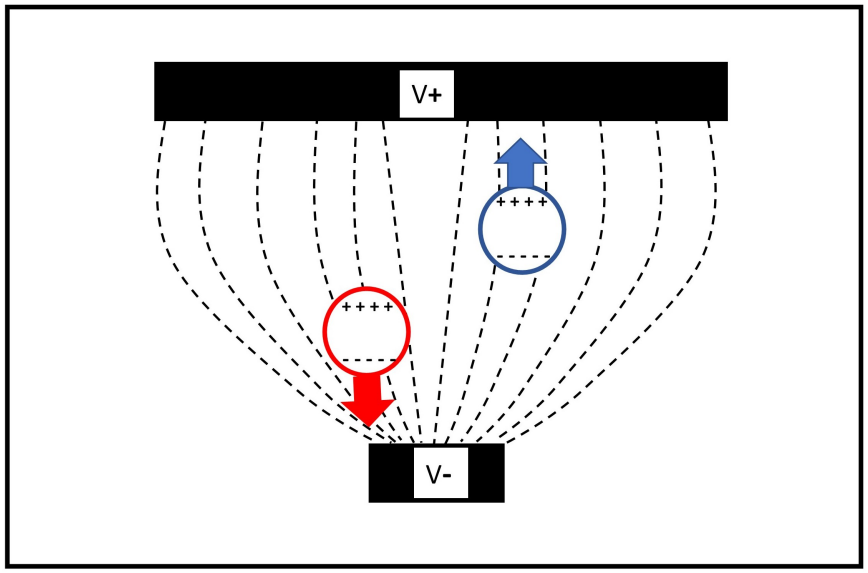

Figure 1.13: A schematic diagram of positive and negative DEP [22].

Particles of similar dielectric constant can be separated by choosing appropriate conductivity and permittivity of the medium [22]. For example,

Markx et al. separated similar bacterial species by using gradients in conductivity [24]. Particles will be in the positive DEP state below a specific frequency and as frequency increases above this specific frequency, particles switch to negative DEP state [22]. This specific frequency is called the cross-over frequency. For different types of particles, the cross-over frequency is different [22]. The DEP force on a particle is expressed as [22],

$$f = 2\pi a^3 \epsilon_m \mathbf{R}e\left(\frac{\epsilon_p* - \epsilon_m*}{\epsilon_p* + 2\epsilon_m*}\right)\Delta E^2 \tag{1.3}$$

where a is the radius of the particle, Δ E defines the electric field gradient, ϵ_m* and ϵ_p* are the complex dielectric constants of the medium and particle. The $\left(\frac{\epsilon_p* - \epsilon_m*}{\epsilon_p* + 2\epsilon_m*}\right)$ factor is called the complex Clausius-Mossotti function that describes the frequency dependence of DEP force [22]. The direction of the DEP force does not depend on the voltage [22]. The dielectrophoresis technique normally applies to microfabricated devices. The DEP force in micro-devices is much stronger than macro-devices making it useful to collect, separate, or manipulate particles.

1.3.2 Dielectric loss

There are two types of heat loss that may dissipate energy in a dielectric material.

- Conducting loss
- Dielectric loss.

Charge flow through the dielectric material causes energy dissipation, which is called conduction loss. In the AC field, dielectric material changes its direction of polarization with time in an oscillating electric field that creates heat energy, which refers to dielectric heat [25]. When an electric field is applied to a dielectric material, the charge distribution of the dielectric material changes and forms a dipole moment. These changes in distribution produce a small current

that causes dielectric loss [25]. As a result, the particle, ion or molecule loses their equilibrium. As the electric field is removed, the dielectric medium tries to regain equilibrium [25]. The time of polarization and reestablishing the equilibrium is not an instantaneous process. The material takes time to respond to an applied electric field. The delay between the applied electric field and polarization to occur is called the relaxation time [25]. The polarization depends on the dielectric constant of a dielectric material. The effective dielectric constant modifies with the change of frequency [22]. So, the amount of dielectric heat depends on the frequency of AC voltage and dielectric constant. The loss is high around the relaxation frequencies of the polarization [25].

1.4 Literature Review

Dielectrophoresis is a popular technique for cell capture and manipulation that is used for various biomedical applications. In 1966, Pohl and Hawk first described how cells respond in a non-uniform electric field [26]. The development of the dielectrophoresis technique was slow until 1980. John Tame was the first to experiment with DEP using micro-fabrication technology [26]. The use of microfabrication to produce microscale electrodes has several advantages. Microelectrodes require less voltage to produce strong DEP force. It is possible to fabricate electrodes of different shapes with very small feature sizes. This new way to fabricate DEP devices accelerated the development of dielectrophoresis technology [26].

Oncology is the study of the diagnosis and treatment of cancer cells. Cancer cells grow abnormally and spread to nearby tissues. The challenges of oncology research include the separation of cancer cells from normal cells, identification of cancer types, and monitoring the progress of cancer treatment [22]. Cancer cells are difficult to detect and separate from healthy cells. Cancer

detection requires expensive equipment for cell sorting, sequencing and highly trained workers are needed to use the equipment [22]. The screening of cancer cells can be improved by combining DEP with a microfluidic platform. The size, shape, and dielectric constant of normal cells and cancer cells differ from each other. Because of their different dielectric constant, cells have different cross-over frequencies, which can be used for characterizing the infected cells [22]. Despite DEP cross-over frequency, the ionic conductivity of the medium has an impact on DEP cell separation [22]. Ionic conductivity of the medium can be adjusted to narrow the AC frequency band [22].

Research on stem cells has become very popular because they can be used in cell therapy, treatment of wounds, drug therapies, and to develop artificial organs [22]. Researchers are using DEP technology to separate stem cells. Fluorescent Activated Cell Sorting (FACS) is a commercial cell sort that requires tedious cell preparation [22]. DEP offers an easy and cost-effective way to identify and differentiate stem cells [22].

DEP technology is useful for drug delivery. Using DEP, the conductivity and permittivity of the membrane and cytoplasm can be determined [22]. DEP has been utilized to observe the drug interaction in the cells by changing the capacitance of the membrane [22]. With microelectrode array, drug treatment responses can be visualized for useful real-time analysis [22]. In drug screening where the supply of cells is limited, the DEP technique can be used as it requires a very small number of cells.

One of the disadvantages of a DEP device is the heating that occurs during its operation. Two mechanisms cause DEP heating:

- Joule heating
- Dielectric heating

Temperature can rise as much as $6^{\circ}C$ because of heating [18]. Joule heating occurs when electrodes are exposed in conductive media. Several experiments have been conducted for minimization of Joule heating by insulating the electrodes and using low conductivity buffer solutions. The measurement of heat associated with the DEP device is a complex task. Commercially available temperature sensors can measure the average temperature in a large area. This is not suitable for measuring local temperatures on a micro-scale device. A thermo-dependent fluorescent dye has been used to measure temperature, but this method leaves chemical residues in the fluid channel that might have a physiological impact on biological cells [27]. Some experiments have been conducted to measure the temperature change and dielectric loss by measuring impedance and resistance as a function of frequency. For example, Glasser et al. measure impedance in the electric field; however, they have used bare electrodes that are in contact with the medium, so in this experiment, only Joule heating was observed [28].

Many temperature sensor technologies are now available for monitoring temperature. However, no single sensor system is right for all applications. The type of sensors and their measurement techniques vary accordingly with the applications. RTD sensors are very popular for measuring local temperatures because of their fast response time, linear resistance-temperature dependency, and high sensitivity. Gallo-Villanueva et al. measure Joule heating effects in insulator-based DEP devices by using a copper RTD sensor [29]. The RTD sensor can be integrated between two electrodes using microfabrication technology to measure the heating effect in a DEP device.

1.5 Approach

In this project, we will observe the dielectric heating loss in DEP operation and measure the spatial temperature change. We will make a DEP device that

consists of two interdigitated electrodes (IDEs) and an RTD sensor between these two electrodes to measure the local temperature rise in DEP operation. The DEP electrodes need to be insulated because when bare electrodes are in contact with the conductive media, Joule heating dominates. A channel is required to pass the fluid media through the insulated DEP.

The DEP electrodes and RTD sensors are made of 40 nm thick nickel metal by a metal evaporation process, on top of a 500 nm thick SiN membrane. A 300 μm thick Si layer is used as a substrate. Si is etched by chemical etching to form the inlet, outlet, and channel. A thin polydimethylsiloxane (PDMS) film is placed on the side of the Si chip to make a microfluidic channel.

A function generator (Keysight 33220 A) is used to supply the AC signal and the signal is amplified by an amplifier (TREK 2100HF) to produce strong DEP forces. The output of the amplifier is connected to the DEP electrodes. An oscilloscope (Keysight DSOX2004A) is also connected with the amplifier output to monitor the applied voltage. The frequency range of the applied AC signal is 100 KHz to 2 MHz. A RTD sensor is connected in a four-wire configuration with Keithley-2400 source/meter unit for measuring accurate resistance change. A LabVIEW program controls all the electronics and collects the data for analysis.

DEP operation and temperature measurement will not be done simultaneously because electromagnetic coupling in the RTD sensor corrupts the temperature measurement. First, we will apply the AC signal in DEP electrodes to produce dielectric loss heating. After some time, we turn off the function generator and then measure the temperature with the RTD sensor. An IR thermal camera is used to visualize the heat that is produced at the time of DEP operation.

1.6 Motivation of research

Temperature influences cell biological response and cellular biochemical reactions [30]. Normal functions of cells and organs are indicated by their temperature [31]. Therefore, in biomedical studies, a better understanding of the effect of temperature in cells is required to understand the metabolism of living cells. In many biomedical applications, the dielectrophoresis technique is used to separate or capture cells because of its strong controllability, easy operation, and high efficiency. In the DEP technique, the gradient of the non-uniform electric field is used to manipulate dielectric particles. The DEP technique causes less damage to the cells compared to conventional microfluidic and mechanical techniques, as it is a contact-free technique to manipulate cell kinetics [32].

Heating has been observed during DEP operation that may have a detrimental impact on living cells. Overheating may cause dehydration, cell membrane disruption, and death of cells [22]. A proper analysis is needed to address the reason and amount of heating. When DEP electrodes are exposed in medium, Joule heating occurs because of the conductivity of the medium. Some researchers have shown a detailed study of reducing the Joule heating by reducing the conductivity of the fluid [18], laminating electrodes by insulation, and modifying the geometry of electrodes [18]. However, when the DEP electrodes are isolated from the medium, the presence of heat is observed that is a function of frequency. The understanding of the heating when electrodes are insulated is very limited. The importance of understanding the origin of DEP heating is the motivation of this research project.

1.7 Thesis outline

This thesis is divided into 5 chapters. The first chapter starts with the importance of temperature sensing and an introduction to dielectrophoresis techniques. Different temperature sensors are introduced with their applications. The importance of measuring heating in DEP operation is also explained in the first chapter. The second chapter deals with the working principle of the temperature sensor and a DEP device. In chapter three, the device fabrication technique and experimental setup are illustrated with schematic diagrams and pictures. All results and related discussions are included in chapter four. Chapter five contains the conclusion and future work of this project. A summary of each chapter is presented below.

Chapter two includes a basic understanding of thermodynamics and temperature-dependent resistance. Different way of heat transfer, heat capacity, and transient heat conduction are briefly discussed in this chapter. At the end of the chapter, the principle of Debye relaxation is described to explain the effect of an AC electric field on the permittivity of a dielectric medium.

Chapter three starts with device fabrication processes including photolithography, etching, metallization and wire bonding. Schematic diagrams are presented to better understand device preparation. The whole device is shown from different directions. The experimental setup for alpha measurement and temperature measurement is presented with a detailed description. In this chapter, images are provided showing device connection with function generator, Keithley 2400, and oscilloscope.

The result of measuring local DEP heat by an RTD sensor and explanation about the reason of this heating are presented in chapter four. A detailed analysis of the result is presented to support our claim. The thermal image of heat in the

DEP device is also included in this chapter. This thesis also includes the conclusion and future work in the last chapter.

CHAPTER 2

PRINCIPLE OF OPERATION

This chapter is intended to explain the basic concept of heat, electrical properties of a conductor, and dielectric heating. The heat transfer mechanism and dielectric heating are explained to understand the temperature change in a DEP device. In this chapter, the polarization, dielectric constant, and Debye relaxation are discussed for a better understanding of the DEP heating mechanism.

2.1 Heat and temperature

The thermal energy of an object describes the energy contained in the motion and vibration of its molecules [33]. The total thermal energy of an object is the combination of its microscopic kinetic energy and potential energy [33]:

$$E_t = E_k + E_p \tag{2.1}$$

where E_t is the total energy, E_k is the kinetic energy and E_p is the potential energy of an object. Heat is a measure of thermal energy that transfers between molecules within a system [34]. Temperature describes the average kinetic energy of molecules within a material or a system [34]. Temperature is a measurable physical property of an object which measures its coldness or hotness [34]. A hotter object has more thermal energy than a cooler object. Thermal energy transfers because of the temperature gradient. The unit of heat is the same as the unit of energy because heat is the flow of energy. According to the second law of thermodynamics, heat flows spontaneously from higher temperatures to lower temperatures [34].

Temperature is measured using the Celsius, Kelvin and Fahrenheit scales. Celsius and Kelvin's scales increase by the same increment; that means a $1°C$ increase results in the same increment of $1K$ temperature. Fahrenheit increases $1.8F$ for $1°C$ increment. At the freezing point, Celsius shows $0°C$, Kelvin $273.16K$, and Fahrenheit $32F$. Kelvin scale is important for scientific calculation. Absolute zero is $0K$ (-273.16°C) temperature, which is the lowest possible temperature that the law of physics allows [34]. The equation for the conversion of different temperature scales is given below.

$$\frac{C}{100} = \frac{K - 273}{100} = \frac{F - 32}{180} \tag{2.2}$$

2.2 Heat transfer

The heat transfer mechanism relies on the basic principle that heat tends to stay at equilibrium or at an equal energy state. The heat transfer rate depends on the temperature difference between two physical systems and the properties of the medium through which the heat is transferred. Heat transfers between two objects in three different ways.

- Conduction
- Convection
- Radiation

2.2.1 Conduction

Heat conduction refers to the transfer of heat from a hot region to a cold region of a material without bulk motion of hot material to the cold region [35]. In a solid material, heat transfers because of the lattice vibration of the molecules and energy transport by free electrons [35]. The basic equation of steady-state heat transfer is called the Fourier law of conduction [35].

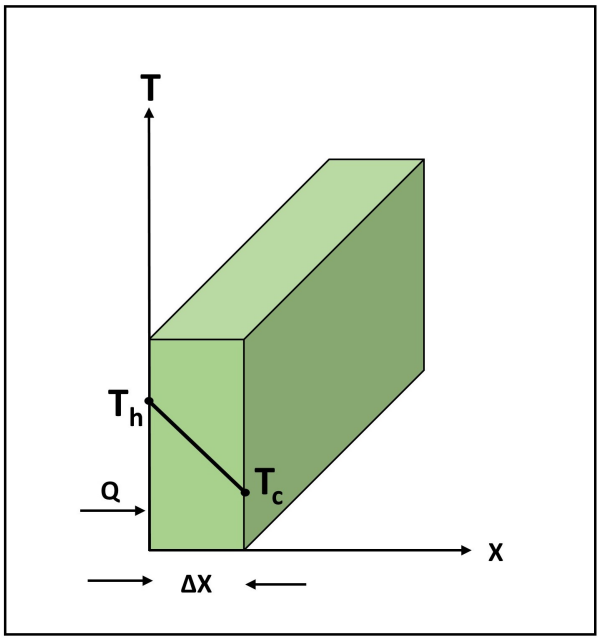

Figure 2.1: One dimensional heat transfer by conduction. Graph reproduced from [35]

Consider a wall of Δx thickness in the X direction, where at x=0, the temperature is T_h, and temperature at x=Δx is T_c as shown in Fig. 2.1. Heat transfer is Q (W) in the direction of X and perpendicular to the plane of temperature difference which is given by:

$$\dot{Q} \propto \frac{A(T_h - T_c)}{\Delta x} \tag{2.3}$$

Or

$$\dot{Q} = \frac{KA(T_h - T_c)}{\Delta x} = -\frac{KA(T_c - T_h)}{\Delta x} = -KA\frac{\Delta T}{\Delta x} \tag{2.4}$$

where K ($\frac{W}{mK}$) is thermal conductivity and A (m^2) is the cross-sectional area of the wall. Conduction thermal resistance (R_{cond}) is represented by:

$$Rcond = \frac{\Delta x}{KA} \tag{2.5}$$

When Δ X$\rightarrow$ 0, the equation reduces to Fourier's law of conduction [35]:

$$\dot{Q} = KA\frac{dT}{dx} \tag{2.6}$$

where dT/dx is the temperature gradient.

2.2.2 Convection

Convection occurs in liquid or gas substance due to the movement of the particles [35]. The motion of fluid occurs due to the difference in density. When fluid is heated up, its density reduces. Therefore, particles from the hot region move to the cold region, and particles from the cold region move to the hot region. The motion will remain until the temperature reaches equilibrium. The heat transfer rate in convection mechanism to/from the surface is given by Newton's law of cooling [35]:

$$\dot{Q} = hA(T_w - T_\infty) \tag{2.7}$$

where h (W/m^2K) is the convection heat transfer coefficient, T_w and T_∞ are the surface and fluid temperature, respectively.

2.2.3 Radiation

Heat can radiate through space without the presence of matter [35]. In this process, energy transfers in the forms of electromagnetic waves. Above the absolute zero temperature, all bodies radiate electromagnetic energy in all directions [35]. The radiated EM wave travels through space until it hits another particle. In space, the electromagnetic wave transports energy at the speed of light. The amount of emitted energy depends on the material, condition, and temperature of the body [35]. A blackbody is a hypothetical surface that is considered as an ideal thermal radiator. It absorbs all radiation energy and emits maximum energy in all directions. The radiated energy per unit area is given by Stefan – Boltzmann law [35]:

$$\dot{Q} = \sigma T^4 \tag{2.8}$$

where σ= 5.67x10^8 Wm^2K^4 is called the Stefan – Boltzmann constant.

2.3 Heat capacity

Heat capacity defines the capacity of a material to absorb heat when it is heated and to release heat when it is cooled [36]. It is defined by

Thermal capacity = mass of body × specific heat

Thermal capacity is the heat required to raise the temperature of a material by one degree. The amount of heat Q(J) absorbed or released by a material is represented as

$$Q = mC(T_2 - T_1) \tag{2.9}$$

where m is the mass of a material (g), $(T_2 - T_1)$ is the temperature difference before and after heating and cooling (K), C is the specific heat of the material ($J/g.K$). The specific heat of a material can be represented as:

$$C = \frac{Q}{m(T_2 - T_1)} \tag{2.10}$$

Specific heat is a measure of heat energy that a unit substance absorbs or releases when temperature increases or decreases 1K [36]. Materials with higher specific heat need more heat energy to increase the temperature.

2.4 Transient heat conduction

Consider an arbitrary shape solid body that maintains a uniform interior temperature through the heating process, as shown in Fig. 2.2. The temperature of this body is a function of time. The heat transfer process based on this model is called lumped system analysis [37].

At t=0, the body is placed into a medium. The temperature of this medium is $T_{ambient}$ and the initial temperature of the solid is T_i. The energy balance of the solid for dt time interval can be expressed as:

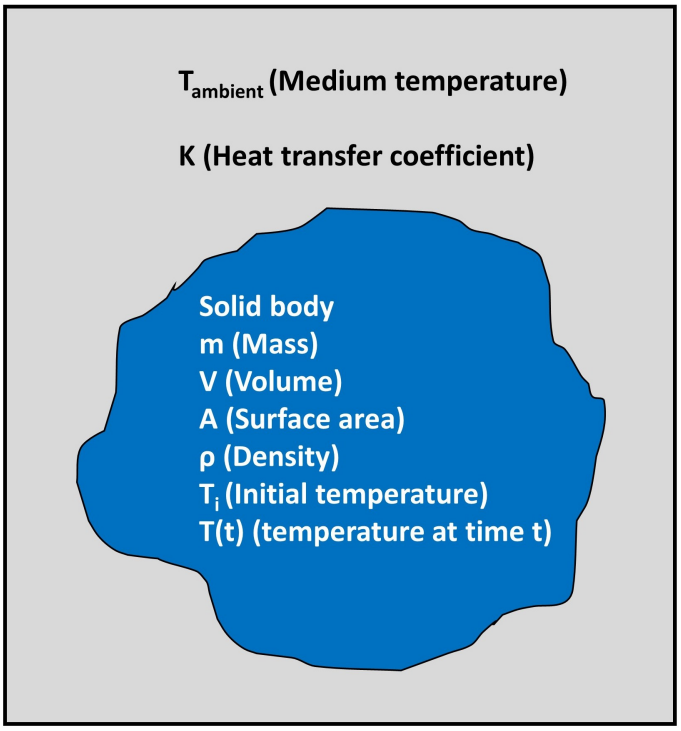

Figure 2.2: Lumped system analysis. Graph reproduced from [38]

Heat transfer into the body during dt = The increase of energy of the body during dt

or

$$KA(T_{ambient} - T(t)) = mC_p dT \tag{2.11}$$

where m is the mass, and C_p is the specific heat of the solid. By changing the variable $dT(t) = d(T(t) - T_{ambient})$ and m=ρV, the equation can be rewritten as:

$$\frac{d(T(t) - T_{ambient})}{T(t) - T_{ambient}} = -\frac{KA}{\rho V C_p} dt \tag{2.12}$$

By integrating Eq. 2.12,

$$\frac{T(t) - T_{ambient}}{T_i - T_{ambient}} = e^{-\left(\frac{KA}{\rho V C_p} t\right)} \tag{2.13}$$

or

$$\frac{T(t) - T_{ambient}}{T_i - T_{ambient}} = e^{-\left(\frac{t}{\tau}\right)} \tag{2.14}$$

or

$$T(t) = T_{ambient} + (T_i - T_{ambient})e^{-\left(\frac{t}{\tau}\right)} \tag{2.15}$$

where $\tau = \frac{\rho V C_p}{KA}$, is called thermal time constant. It represents the time required for the body to reach 63.2% of the final specified temperature [37]. The thermal time constant can be interpreted as [37]:

$$\tau = \frac{1}{KA}(\rho V C_p) = R_t C_t \tag{2.16}$$

where R_t is the resistance to convection heat transfer and C_t is the lumped thermal capacitance of the solid.

2.5 Resistance

According to Ohm's law, electrical current is proportional to the voltage and inversely proportional to the resistance of the conduction. Electrical resistance is a quantity that measures the hindrance of charge flow through the circuit. The resistance of an object depends on its shape and constituent material. In a cylindrical conductor, electrical resistance R is directly proportional to the length (L) of the resistor and inversely proportional to the cross-sectional area. The longer the conductor, the more collisions occur between charges and atoms. The greater the cross-sectional area of the conductor, the more charges can transmit through it. The electrical resistance is given by:

$$R = \frac{\rho L}{A} \tag{2.17}$$

where ρ ($\Omega.m$) is the resistivity of a material. The resistivity is an intrinsic property of a material. Since conductors have large free charge density, their resistivity is low. Whereas insulators have high resistivity because most of their charges are bound to atoms. Table. 2.1 shows the resistivity of different bulk materials at 20°C.

Material	Resistivity ρ ($\Omega.m$)
Aluminum	2.82×10^{-8}
Constantan	4.9×10^{-7}
Copper	1.68×10^{-8}
Iron	1.0×10^{-7}
Nickel	6.99×10^{-8}
Platinum	1.06×10^{-7}
Titanium	4.20×10^{-7}
Zinc	5.90×10^{-8}

Table 2.1: Resistivity of different bulk materials at 20°C [39].

2.6 Temperature-dependent resistance

The electrical resistance of a material is a function of temperature. There are two reasons for the temperature-dependent resistance change. For some materials, resistance increases as temperature increases due to the increase of the number of collisions between charges and atoms. However, some materials such as semiconductors, resistance decreases as temperature increases due to the increase of free charges. The temperature-dependent resistance can be determined by the given formula:

$$R_T = R_o(1 + \alpha_T \times T) \tag{2.18}$$

where R_T is the resistance at $T°C$, R_0 is the resistance at $0°C$, and α_T is the temperature coefficient at $0°C$. Temperature coefficient (α) of a material measures the change of resistance per degree of temperature change. The value of α is positive for metal because the resistance increases at higher temperatures. For semiconductors and some non-metals, the alpha value is negative due to resistance decrease at higher temperatures. The alpha value can be measured by measuring two resistance (R_1, R_2) at two different temperatures (T_1,T_1).

At T_1 temperature,

$$R_{T_1} = R_o(1 + \alpha \times T_1) \tag{2.19}$$

At T_2 temperature,

$$R_{T_2} = R_o(1 + \alpha \times T_2) \tag{2.20}$$

Division of Equ. 2.19 and Equ. 2.26,

$$\frac{R_{T_1}}{R_{T_2}} = \frac{1 + \alpha \times T_1}{1 + \alpha \times T_2} \tag{2.21}$$

or

$$\alpha = \frac{R_{T_1} - R_{T_2}}{R_{T_2}T_1 - R_{T_1}T_2} \tag{2.22}$$

The value of alpha for different bulk materials at $20^{\circ}C$ is shown in Table 2.2.

Material	Temperature coefficient α
Aluminum	0.004308
Constantan	-0.000074
Copper	0.004041
Iron	0.005671
Nickel	0.005866
Platinum	0.003729
Tungsten	0.004403
Zinc	0.003847

Table 2.2: Temperature coefficient of different bulk materials at $20^{\circ}C$ [40].

2.7 Dielectric materials and polarization

Atoms are a composition of the positively charged nucleus and one or more electrons surrounding the nucleus. In the insulators, all electrons are bound in the atomic molecular orbit and there are no free electrons to move around. Therefore, dielectric insulators contribute no current under an applied electric

field. When a dielectric material is placed under an electric field, its positive charges move slightly in the direction of the electric field and negative charges move slightly in the opposite of the electric field [41]. The formation of this dipole is shown in Fig. 2.3. The distorted atomic orientation with a net dipole moment is called the electric polarization [41].

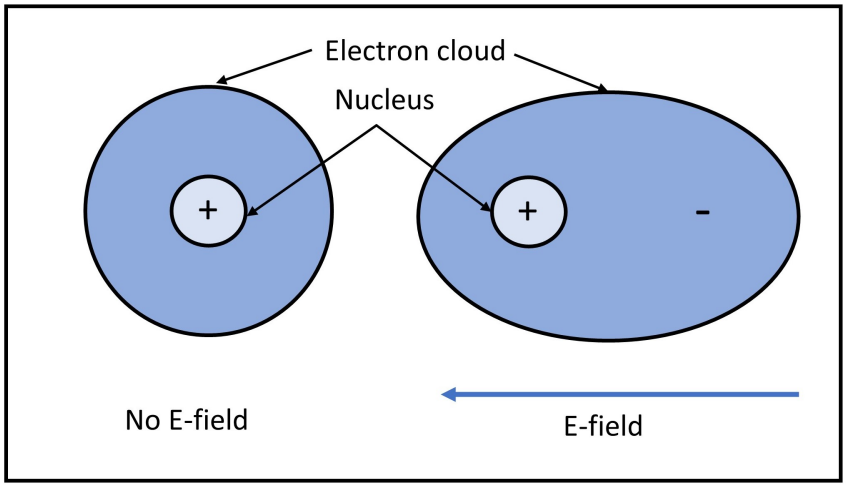

Figure 2.3: Dipole in an applied electric field

Polarization reduces the electric field within the dielectric material. The dipole moment of two charges +Q and -Q separated by distance $\vec{d}$ can be represented as,

$$\vec{p} = Q\vec{d} \tag{2.23}$$

The polarization $\vec{P}$ (C/m^2) is the measure of the net dipole moment which is represented by:

$$\vec{P} = NQ\vec{d} \tag{2.24}$$

where N is the number of charge dipoles per unit volume in the material. The polarization is proportional to the strength of the electric field [41]. The direction

of polarization is toward the direction of the electric field.

$$\vec{P} \propto \vec{E} \tag{2.25}$$

$$\vec{P} = \varepsilon_0 \chi_e \vec{E} \tag{2.26}$$

where ε_0 is absolute permittivity that is defined as how much resistance is encountered for forming an electric field in the vacuum and χ_e is the electric susceptibility that measures how easily a dielectric material polarizes in an applied electric field [41]. χ_e is related to the relative permittivity as $\varepsilon_0 = 1 + \chi_e$ [41]. The relative permittivity is a ratio of the permittivity of a given material to the permittivity of a vacuum [41].

2.8 Debye relaxation

The dielectric properties of materials are usually described by two constants ϵ' and ϵ'' which are called dielectric constants or loss factor [41]. They can be combined in a complex dielectric constant given by:

$$\epsilon = \epsilon' - j\epsilon'' \tag{2.27}$$

In 1929, Debye proposed a model to explain dielectric relaxation for some materials [41]. Debye showed the complex dielectric constant as a function of field frequency (ω) [41]:

$$\epsilon(\omega) = \epsilon_\infty + \frac{\epsilon_\infty - \epsilon_0}{1 - j\omega\tau_d} \tag{2.28}$$

where ϵ_0 is the permittivity at frequencies below dipole relaxation, and ϵ_∞ is the permittivity at frequencies above dipole relaxation, and τ_d is called characteristic relaxation time of the medium or Debye relaxation time constant. The complex dielectric constant can be separated into real part and imaginary part as [41]:

$$\epsilon' = \epsilon_\infty + \frac{\epsilon_\infty - \epsilon_0}{1 + \omega^2 \tau_d^2} \tag{2.29}$$

$$\epsilon'' = (\epsilon_\infty - \epsilon_0) \frac{\omega \tau_d}{1 + \omega^2 \tau_d^2} \tag{2.30}$$

where real part of the permittivity ϵ' is called AC capacity and imaginary part of the permittivity ϵ'' is called the dielectric loss factor.

CHAPTER 3

DEVICE FABRICATION AND EXPERIMENTAL METHODS

Micro electromechanical system (MEMS) refers to the fabrication of devices where at least some of their dimensions are in the range of micrometer [42]. MEMS fabrication involves many critical steps. In this chapter, the device fabrication processes are reviewed and the experimental setup is described for measuring the temperature coefficient and temperature of DEP device.

3.1 Device preparation

We have prepared a device that consists of two interdigitated electrodes (IDEs) and an RTD sensor in between these two electrodes. The electrodes and an RTD sensor are fabricated on top of a 500 μm thin SiN membrane. The thin SiN membrane reduces thermal mass significantly, which increases the sensitivity of the RTD sensor and reduces the thermal time constant, which results in a faster measurement [43]. Details of the device fabrication steps are given below.

3.1.1 Mask preparation

A photomask is a nearly optically flat glass or quartz plate that has a chromium absorber pattern on it that is used to transfer patterns on resist-coated wafers repeatedly [42]. The glass and quartz are transparent to UV light, whereas the chromium pattern is opaque to UV light. The mask is placed on top of the photoresist-coated surface and then exposed to UV radiation. The fabrication process of photomask involves several steps.

Step 1: Data preparation

A drawing package is needed to create a pattern. In this step, designs or layers translate in a form that can physically write the design by photomask writer. A drawing program such as AutoCAD, Canvas, Freehand, Adobe-Illustrator, or L-Edit can be used to design the pattern [42]. In our case, we use L-edit to design the pattern, and the photomask data is prepared in GDSII format.

Step 2: Exposure

The designed pattern is transferred using a laser writer, an LED writer, or an e-beam writer. In our case, we use the Heidelberg instruments "MLA-100". This optical system can write down a 1 μm line at a speed of 50 mm^2/min. As a light source, we use an LED of 365 nm wavelength. A 5 inch$\times$5 inch telic mask is used that is coated with 530 nm thick AZ1500 photoresist. In this step, the blank photomask is placed in a stage where the photomask writer exposes UV light. The light-sensitive photoresist absorbs the UV light and creates an image.

There are 2 types of photoresists.

- Positive photoresist
- Negative photoresist

For positive photoresist, the exposed portion dissolves in the developer and washes away. For negative photoresist, the exposed portion becomes insoluble and the unexposed portion dissolves in the developer. AZ 1500 is a positive photoresist.

Step 3: Develop

After exposure, the photoresist needs to develop to show the pattern by washing away the weak photoresist region. We use a mixture of AZ-400K and water in a 2:1 ratio to make a developer. It takes about 1 min to develop the pattern. After developing the mask, it rinses in DI water. Then we dry the mask by blowing nitrogen on it. We check the pattern of the developed mask in a microscope.

Step 4: Etching

We use a chemical etching process to etch chromium selectively from the photomask. Chromium etchant takes less than 30 sec to etch away chrome from uncovered PR surface. The mask patterning needs control processing to avoid undercut or overcut etching. After etching chromium, the mask is washed several times with DI water so that no residue is left on the surface.

Step 5: Photoresist stripping and mask cleaning

The leftover photoresist needs to be removed from the mask to avoid polymer-polymer contact when the mask and wafer are in contact for UV exposure. Polymer contact can create friction that can tear away the photoresist from the wafer at the time of alignment. The photoresist dissolves in acetone or 1165 solvent. The mask is placed in a bikar with 1165 for 30 mins at $70^{\circ}C$ to remove the photoresist. To assure the photoresist is completely removed, the mask is further cleaned with plasma cleaning. After removing the photoresist, the mask is cleaned in DI water several times and dried with nitrogen blow.

We made two masks for fabricating our device. One is for membrane pattern and the other is for electrode pattern. When Chromium stays only in the

pattern region of the mask, the mask polarity is called light field. When Chromium etches only from the pattern, the mask polarity is called dark field. The membrane mask polarity is dark field, and the electrode mask is light field. Fig. 3.1 demonstrates the light field and dark field polarity of a mask.

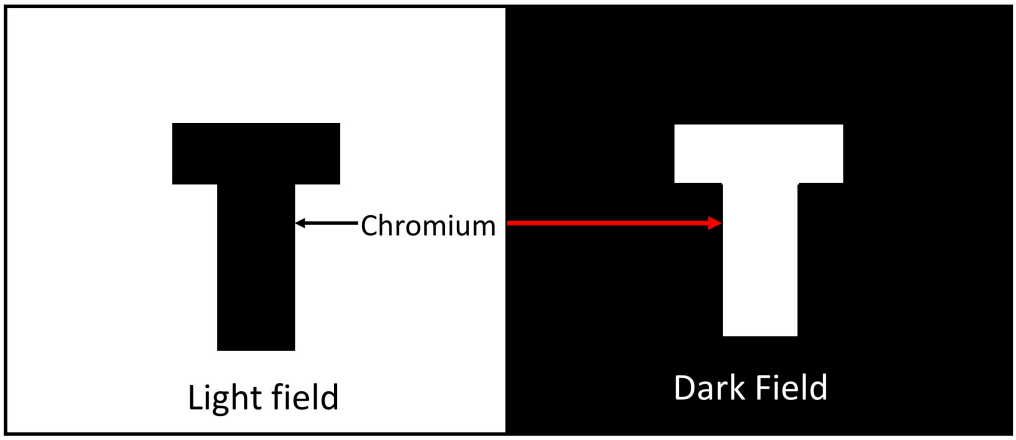

Figure 3.1: Light field and dark field polarity. Graph reproduced from [42]

3.1.2 Wafer preparation

We have used 300 μm thick (100) oriented single crystal Si wafer. The top and bottom surface of the wafer is covered with the SiO_2 and SiN layer. The wafer preparation includes

- Oxidation
- SiN deposition

Details of these two processes are given below.

Oxidation

Thermal oxidation is a process to produce silicon dioxide on the surface of Si. At elevated temperature (between 600 and 1250$^{\circ}C$), the chemical reaction

between oxygen and Si produces SiO_2. Even at room temperature Si readily oxidizes, forming a 2 *nm* thick oxide layer. High temperature accelerates the diffusion of oxidant through the surface oxide layer to the Si interface to grow thick oxides. The ambient of thermal oxidation can be wet or dry, depending on using water vapor or molecular oxygen as the main oxidant. The reactions of wet and dry oxidation are given below,

$$Si + 2H_2O = SiO_2 + H_2O(wet) \tag{3.1}$$

$$Si + O_2 = SiO_2(dry) \tag{3.2}$$

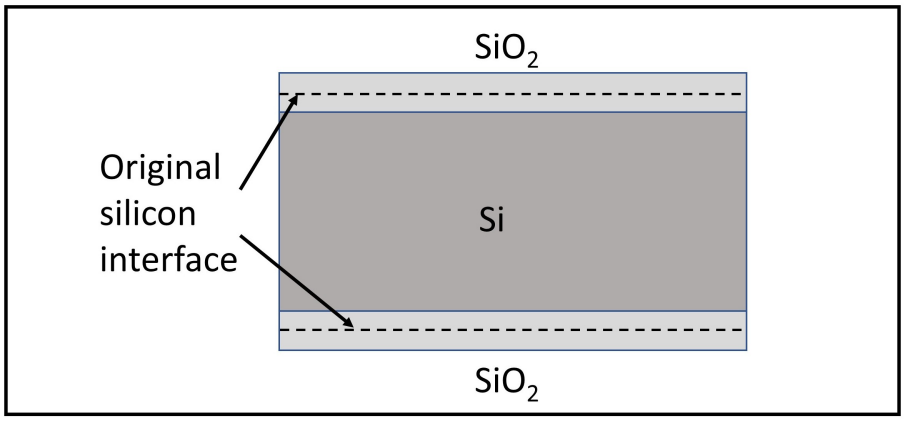

Figure 3.2: Silicon thickness conversion. Graph reproduced from [42]

The ratio of silicon converted into oxide is 0.46. Fig. 3.2 shows the conversion of silicon thickness into oxide. Silicon dioxide layer is mainly used for insulation, as a sacrificial layer, and masking. The quality of silicon dioxide depends on its growth method. Better quality oxide is produced in the dry oxidation method. High temperatures and pure oxygen can produce high density and pinhole-free oxide layer. Wet oxidation can produce oxide faster because OH^-

ion can diffuse faster through the grown oxide layer than O_2. The water causes a losing effect on SiO_2 that makes it impurity prone. Because of its fast rate, wet oxidation is used where thick oxide is required. In our case, we use the wet oxidation process. Fig. 3.3 shows the oxidation setup. Steps of the oxidation process are described in the following list:

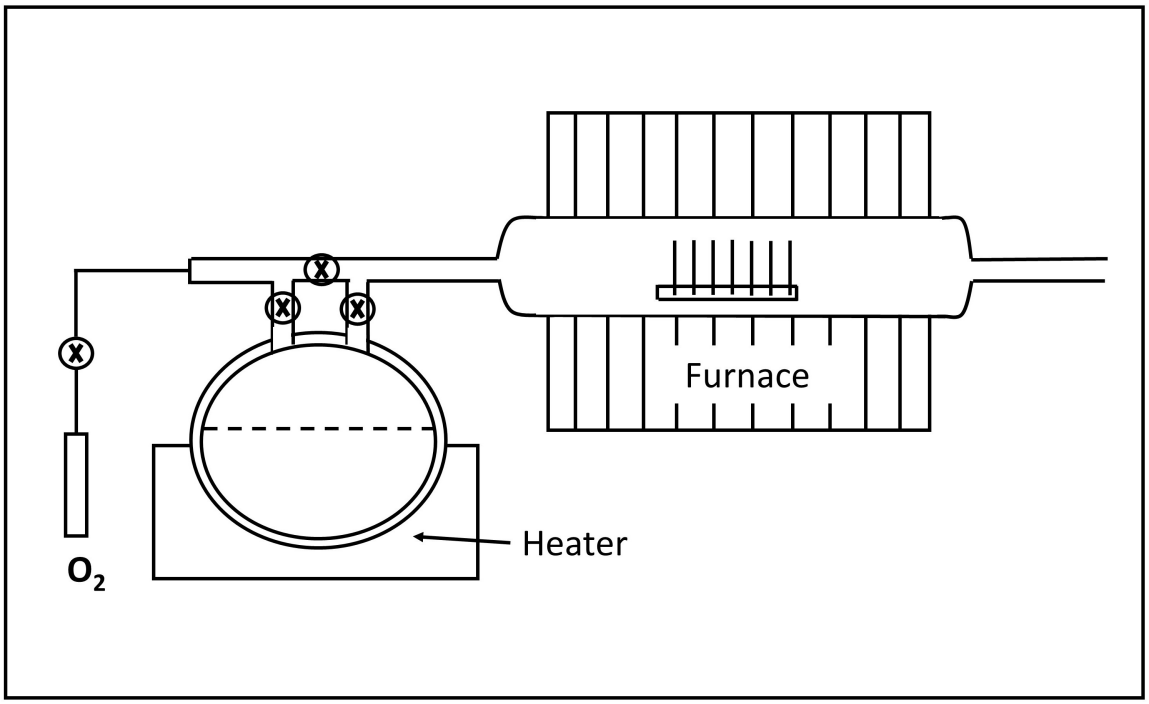

Figure 3.3: A schematic diagram of wet oxidation setup. Graph reproduced from [42]

1. The wafer is placed inside the furnace boat and temperature is set 920°*C*.
2. We turn on the water boiler when the temperature of the furnace reaches 800°*C* and set the boiler temperature to 90°*C*.
3. As the temperature of the furnace reaches 920°*C* and the boiler starts to boil water, the oxygen starts to flow through the boiler to the furnace.

4. The oxidation rate is about 0.2 μm/hr, and the time is about 1 hour. So, the thickness of the SiO_2 layer is about 200 - 250 nm.
5. After 1 hour, we switch off the oxygen valve and turn off the furnace. The furnace cools down to room temperature within 24 hours, and then we take out the wafer.

SiN deposition

In microfabrication, SiN is used for its superior mechanical, chemical, and electrical properties [42]. SiN is an insulator material ($10^{16}\Omega$-cm) [42]. The Young's modulus of SiN is higher than Si [42]. It provides an efficient passivation barrier to the diffusion of water molecules [42]. In many etchants, It has a highly selective etch rate over SiO_2 and Si [42]. In our application, the SiN layer serves as a mechanical membrane and as an isolation layer. SiN can be deposited by low-pressure chemical vapor deposition (LPCVD) or plasma-enhanced chemical vapor deposition (PECVD) techniques. We have used the LPCVD technique to deposit a SiN film on top of the 250 nm thick SiO_2 layer. In the LPCVD technique, SiN is deposited at 700-800$^\circ C$ and 200-500 mTorr pressure [42]. In this process, SiN is deposited from silane or dichlorosilane and ammonia in a reaction such as [42]:

$$3SiCl_2H_2 + 4NH_3 = Si_3N_4 + 6HCl + 6H_2 \tag{3.3}$$

Using dichlorosilane instead of silane gives more uniform film thickness [42]. The film stress can be controlled by increasing or decreasing the Si content in SiN. We prepare a high-stress nitride film by reducing the Si content. The thickness of the SiN film is about 500 nm.

3.1.3 First lithography

A photolithography process is analogous to a photographic process where negative is developed to create a pattern. Photolithography involves a set of steps that need to be done with care to get more yield. The details of this process are described below.

Surface conditioning

The wafer surface needs to be prepared before coating with photoresist. Particles on the wafer surface can create problems to adhere to photoresist and to get a uniform thickness of photoresist. Therefore, the wafer surface needs to be cleaned thoroughly. The wafer surface is coated with an intermediate buffer that promotes the adhesion of photoresist to the surface. We use HMDS (Hexamethyldisalizane) that creates a hydrophobic surface where photoresist can adhere well. Three basic steps are followed to prepare the wafer surface: baking, primer coating (HMDS), and cooling.

After cleaning the wafer, the existing water molecules must be removed. The wafer is heated to $200^{\circ}C$ to remove the water molecules. The wafer is then coated with a monolayer of HMDS by the chemical vapor deposition process. As HDMS creates a hydrophobic surface, the water molecules will not reaccumulate on the surface once the wafer returns to the environment. The wafer is cooled down to room temperature.

Spin coating

Spin coating is the most common coating process used to coat photoresist. We have used AZ-5214E, a positive photoresist. The wafer is placed on the wafer holder of the spinner. The photoresist is applied by using a pipet. As the spinner

starts to spin, it throws the excess photoresist away and gives a uniform resist thickness. It continues to spin until most of the solvent evaporates.

Soft bake

The wafer is then soft baked under $110^{\circ}C$ to remove all residual solvent of photoresist. After soft bake, the wafer is cooled down to room temperature.

UV expose

Before exposure, the wafer is aligned with a mask. Alignment is one of the most important steps in the microfabrication process. A small misalignment can destroy all the devices of the wafer. The wafer is placed on the chuck of the aligner and using x, y stage the wafer is aligned with the mask. Three different printing methods are used in microfabrication:

- Contact printing
- Proximity printing
- Projection printing

In contact printing, the mask is pressed against the wafer with 0.05 to 0.3 atm pressure [42]. Fig. 3.9 illustrates the contact printing process. The resolution of contact printing depends on the light wavelength and the thickness of the photoresist [42]. High resolution can be achieved by using a shorter wavelength and a thinner resist layer [42]. Contact printing can damage and contaminate the mask.

In proximity printing, the wafer and photomask keep a space between them that reduces damage to the photomask. However, the diffraction of transmitted light reduces the resolution [42]. The resolution of proximity printing depends on the separation distance between the mask and wafer. Typical mask

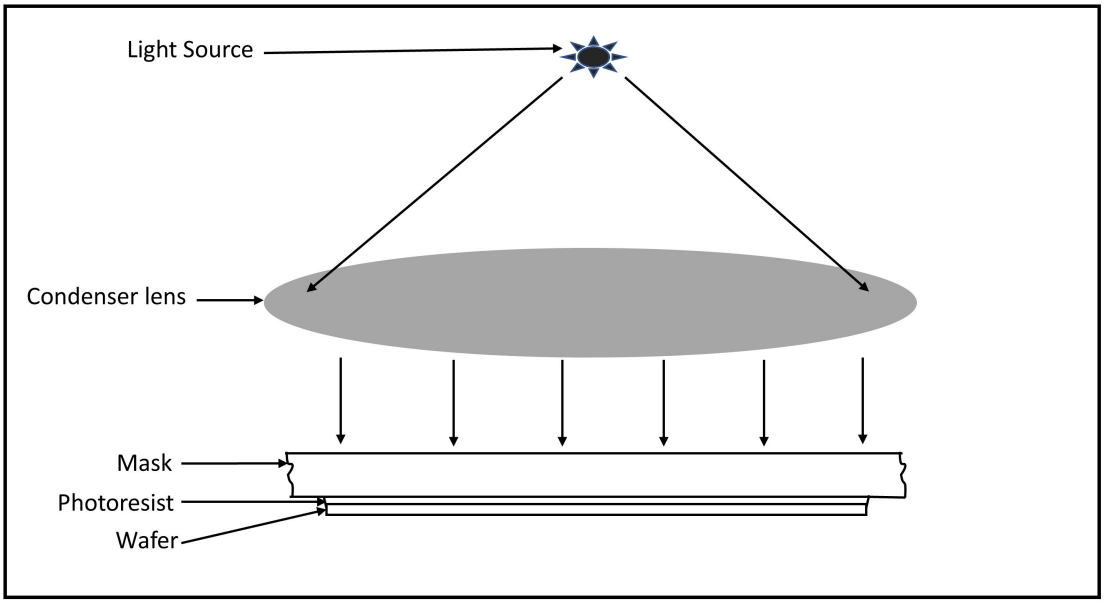

Figure 3.4: A schematic diagram of contact printing. Graph reproduced from [42]

and wafer separations are 20 to 50 μm [42]. The smallest features of UV proximity printing are about 2-3 μm [42].

Contact between the wafer and photomask is also avoided in projection printing. A high-resolution lens projects an image of the mask on the surface of the wafer [42]. The limiting resolution of projection printing depends on the wavelength of light, the numerical aperture of the imagining lens system, and mask aligner optics [42].

We have used the contact printing method to expose the wafer. A 100 W and 395 *nm* wavelength UV LED is used as a light source. We have aligned the wafer to mask using the x, y stage. We have exposed the photoresist for 15 sec in UV light.

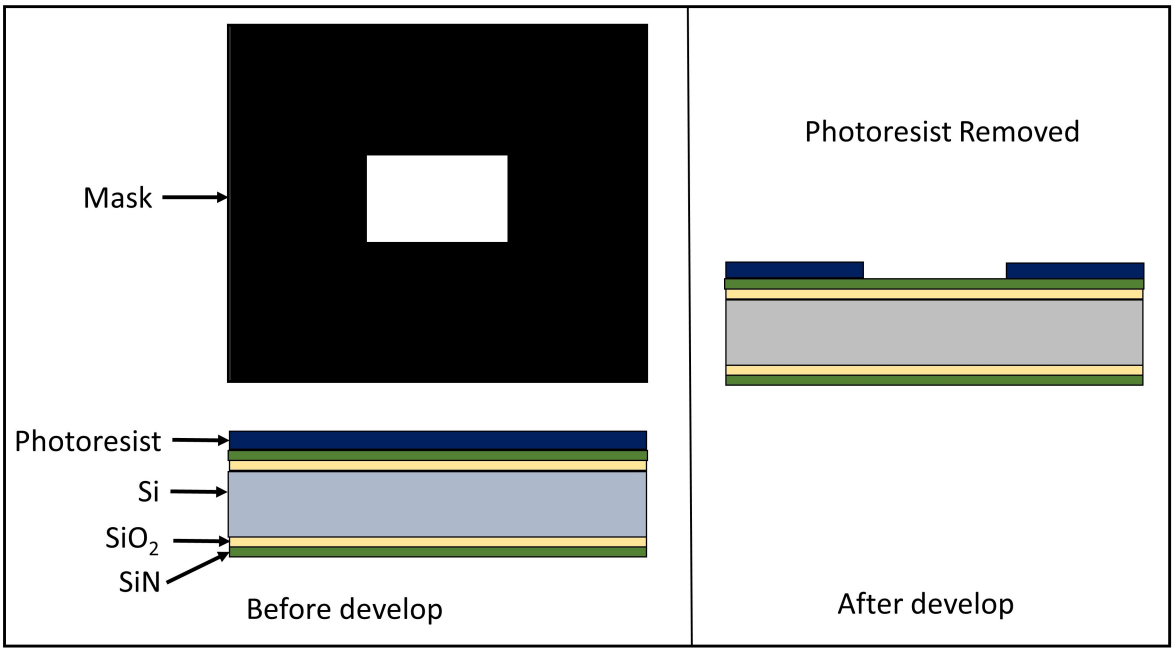

Figure 3.5: The profile of a positive resist before and after development.

Develop

The pattern is developed by a wet chemical process. A mixture of AZ-400K developer and water in a 4:1 ratio is used to develop our pattern. The wafer is placed in a bikar with the developer solution. Developing time is very important in microfabrication. A long developing time can lead to overdeveloped resist, and a very short time can lead to underdeveloped resist. We develop the pattern for 1 min. After developing the pattern, the wafer is rinsed in DI water to stop the chemical reaction. Since we have used positive resist, the exposed resist is dissolved in the developer and unexposed resist remains on the wafer. Fig. 3.5 demonstrates the profile of a positive resist before and after development. The wafer is then dried and kept for further processing.

3.1.4 Etching

The etching process is important to make functional MEMS structures. In our work, we need to etch SiN, SiO_2, and Si to create a SiN membrane. There are two classes of etching [44]:

- Wet etching
- Dry etching

We have used a dry etching process to etch SiN and wet etching process to etch SiO_2 and Si. Details of the etching process that are used in our work are given below.

SiN etching

We have used the reactive ion etching (RIE) process to etch SiN. In reactive ion etching, the wafer is placed inside a chamber where pressure is 700 mTorr. Inside the chamber, plasma is created by an RF power source that breaks the gas molecules into ions [44]. In RIE, atoms are etched from the surface both chemically and physically [44]. In chemical etching, ions are accelerated towards the wafer and react selectively with surface atoms, forming another gaseous material [44]. The physical etching process is like the sputtering deposition process. When ions accelerate with high energy, they can knock out the atoms without chemical reaction [44]. Physical etching can reduce the thickness of the photoresist. Therefore, RIE can damage the pattern of the wafer if it runs for a long time. A schematic diagram is shown in Fig. 3.6, illustrating the reactive ion etching system. We have used CF_4 gas to etch SiN in RIE. The etching rate of SiN is 10 $nm/$min. CF_4 gas can etch SiO_2 and Si chemically. Therefore, a long time etching with CF_4 gas can etch away SiO_2 and Si.

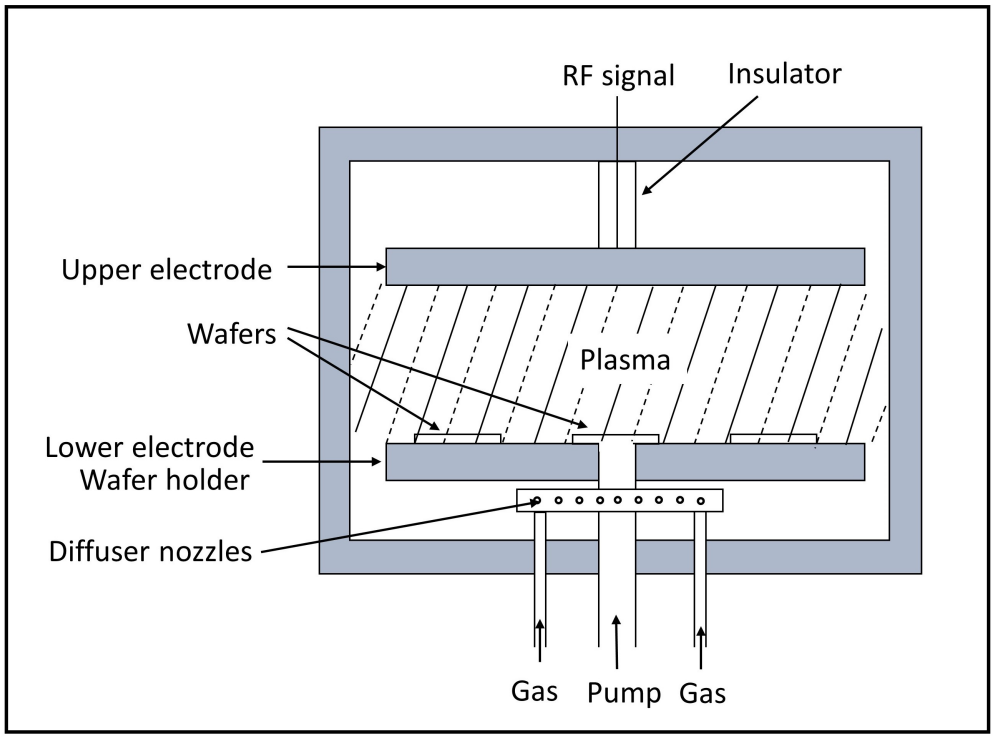

Figure 3.6: A schematic diagram of the reactive ion etching system. Graph reproduced from [44]

SiO_2 etching

SiO_2 film can be etched by using buffer oxide etchant (BOE) or hydrofluoric acid (HF). HF and BOE are both highly selective chemicals for SiO_2. HF can etch SiO_2 very rapidly, making it difficult to control the etching rate, and hence undercut may occur [45]. A buffered oxide etchant is a mixture of hydrofluoric acid and ammonium fluoride. BOE has a slow and constant etch rate, which is desirable for opening the mask window for a silicon substrate [45]. The etching reaction of SiO_2 and HF is given below [45]:

$$SiO_2 + HF = H_2SiF_6 + 2H_2O \tag{3.4}$$

H_2SiF_6 is soluble in water. We have used a BOE containing HF and NH_4F in a 1:6 ratio. The etch rate is 100 nm/min at 21°C. We have placed the wafer in a BOE solution. As SiO_2 etches away, a grey color appears because of the underlying Si surface. After etching SiO_2 with BOE, the surface becomes highly hydrophobic.

Si etching

We have used 30% KOH solution to etch Si. It is an anisotropic etching because the etching rates of Si are different for different crystal planes. Si atoms are etched more rapidly in the {100} and {110} planes [42]. The etch rate of the {111} plane is very low, therefore the {111} plane acts as etch stops [42]. The etch rate of the {100} plane in 30% KOH solution at 60°C is about 0.4 μ/min. The chemical reaction between KOH and Si is given below [42]:

$$Si + 2OH^- + 2H_2O = Si(OH)_4 + H_2 = SiO_2(OH)_2{}^{-2} + 2H_2 \tag{3.5}$$

In a high water concentrated solution, the production of $Si(OH)_4$ is very fast [42]. Before $Si(OH)_4$ can diffuse away, it may form a SiO_2-like complex. Then a white residue may be observed on the wafer surface [42]. We have placed the wafer in a bikar with 30% KOH solution. This bikar is placed in a hot water bath to heat it up to roughly 60°C. The water bath is located on top of a stirrer to mix KOH with water solution. The stirrer is set on 220 rpm. Fig. 3.7 shows the setup of KOH hot water bath.

The etch rate of SiO_2 is fast in the presence of KOH [42]. So underlying SiO_2 is etched away in a hot KOH bath. The wafer profiles after each etching process are shown in Fig. 3.8. After the etching process, the SiN membrane is formed in the patterned area.

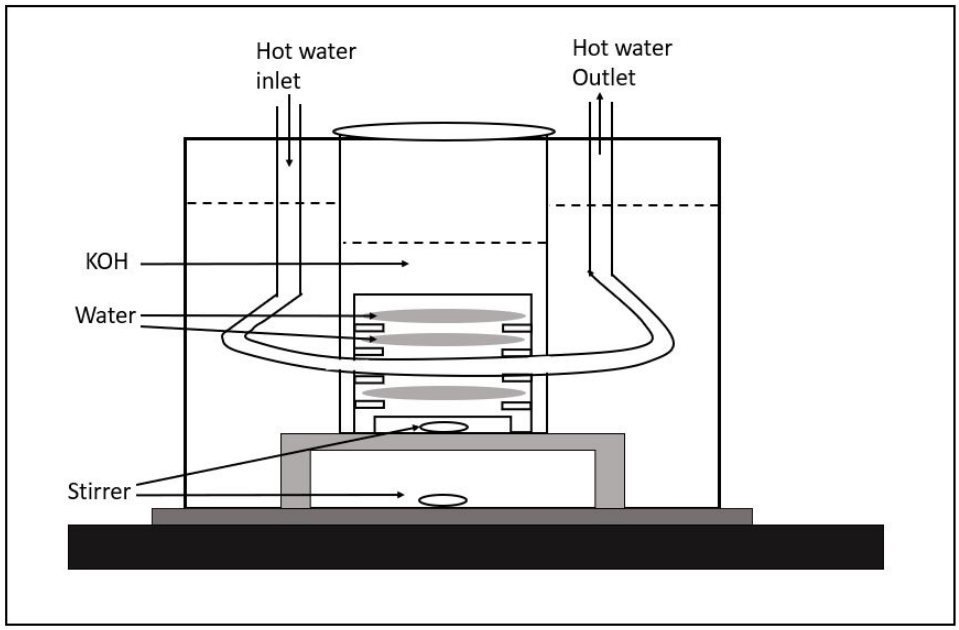

Figure 3.7: A schematic diagram of KOH hot water bath.

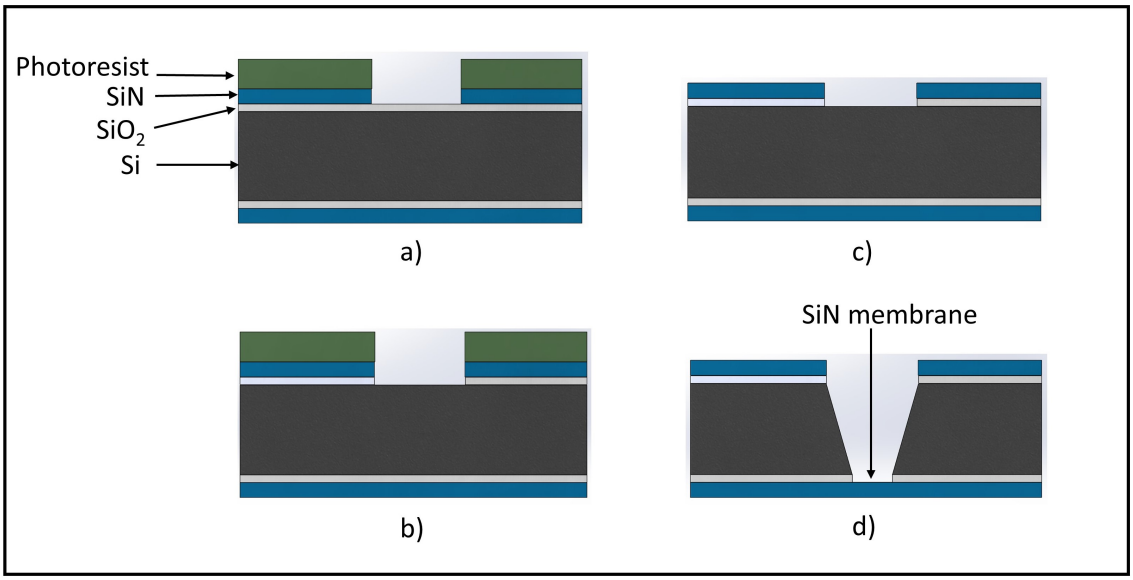

Figure 3.8: The wafer profile a) after SiN etch b) after SiO_2 etch c) after removing resist d) after Si etch.

3.1.5 Second lithography

In the second lithography, the metal pattern is transferred to the wafer surface where the membrane is formed. We have followed the image reverse lithography technique to transfer the pattern in the wafer. Image reverse lithography is useful in some applications where it is difficult to make narrow electrodes by using a wet chemical etching process because of undercut photoresist [46]. However, the image reverse process is more time consuming because of its additional process steps. Compared to positive lithography, image reverse process requires additional baking and flood exposure steps. The image reverse steps are given below:

1. In the image reverse lithography process, the steps up to soft bake are the same as positive lithography steps. The wafer is exposed for 7 sec under the photomask. In this case, we have used a light field photomask.
2. After exposure, the wafer is heated up to around $120^{\circ}C$. In this image reversal bake step, exposed photoresist loses its ability to develop, while unexposed photoresist remains photoactive [46].
3. The wafer is then flood exposed for 15 sec. During the flood exposure, the photoresist areas which have not yet been exposed are also exposed and can be developed in a developer solution [46].
4. The wafer is developed for 1 min in the developer solution. Fig. 3.9 shows the profile of photoresist in different image reverse steps.

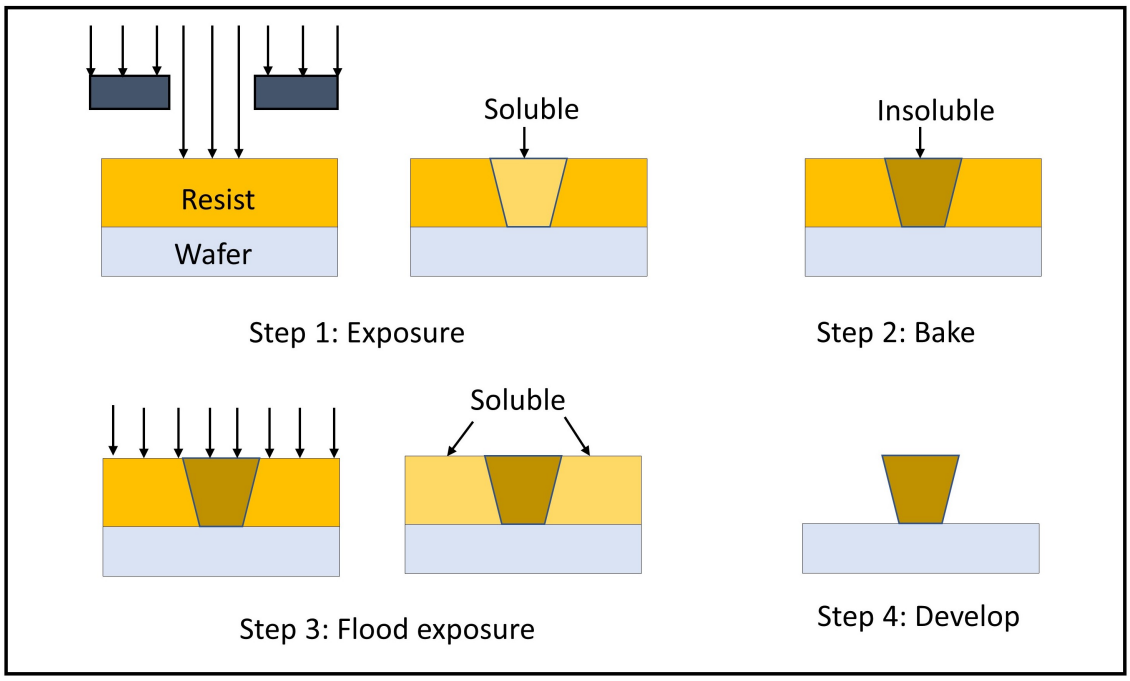

Figure 3.9: The profile of photoresist in different steps of image reverse process. Graph reproduced from [47]

3.1.6 Metallization

We have used the thermal evaporation process to produce a thin metal film in the wafer. In this process, metal is boiled off onto a substrate [42]. From thermodynamics, the number of molecules leaving from a unit area of evaporant per unit second or flux F is given by [42],

$$F = N_o \exp \phi / KT \tag{3.6}$$

where ϕ is the activation energy needed to evaporate one molecule of the metal. In the laboratory, the evaporation is carried out by the resistive heating method [42]. A high current passes through a metal structure which is called filament or boat [42]. The heated filament is used to evaporate the source metal. The evaporation process is carried out inside a vacuum chamber [42]. The wafer is

placed on a substrate holder situated on top of the source heater. Fig. 3.10 shows a schematic diagram of thermal evaporation system. A high vacuum is needed so

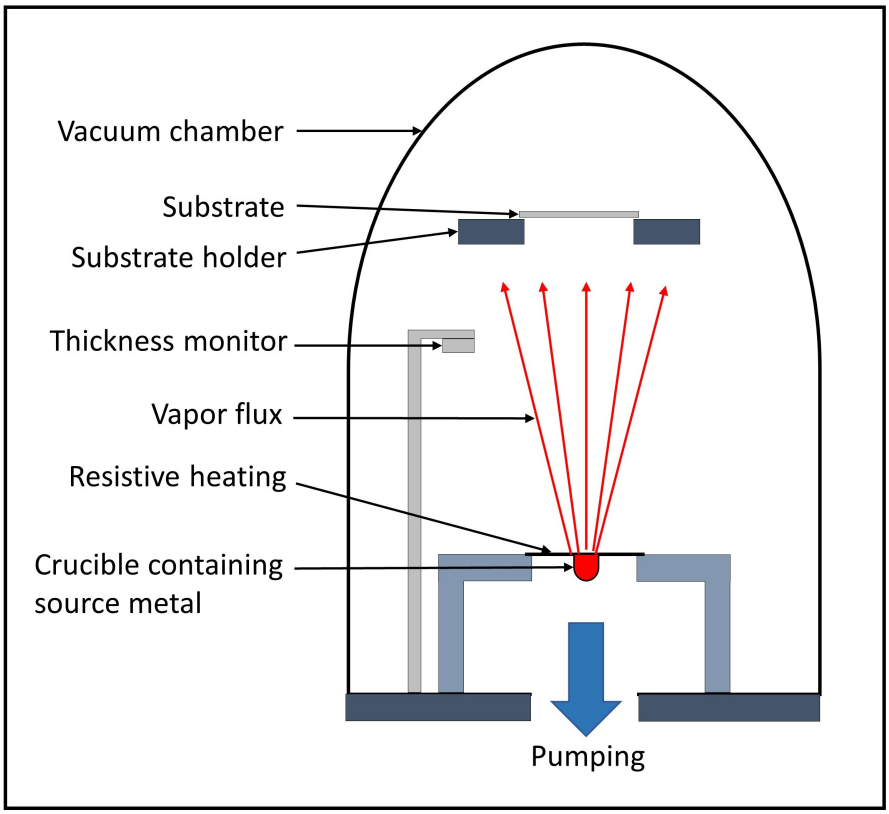

Figure 3.10: A schematic diagram of thermal evaporation system. Graph reproduced from [42].

that most atoms/molecules will deposit on the wafer without suffering collisions with other gas molecules [42]. The fraction of particles scattered by collisions is proportional to [42]:

$$1 - \exp\left(d/\lambda\right) \tag{3.7}$$

where d is the distance between source and wafer, and lambda is the mean free path of the particles. At 10^{-5} torr, the mean free path is about 5 m [42]. In our thermal evaporation system, the pressure is about 9x10^{-7} torr. The distance

between source and wafer is about 40 cm. For metallization, we have used the lift-off process. After developing the pattern, we have deposited 25 nm nickel metal on the wafer surface using thermal evaporation technique. The wafer is then kept in microposit remover (1165) at 70°C for one hour to remove the photoresist. As photoresist dissolves in 1165, the metal on top of the photoresist also comes off the wafer. The metal which is deposited directly on the surface of the wafer has remained after the lift-off process. Fig. 3.11 shows the profile of metal during the lift-off process. The wafer is then cleaned with DI water and dried by flowing N_2 gas. The sensor electrodes are inspected by a microscope.

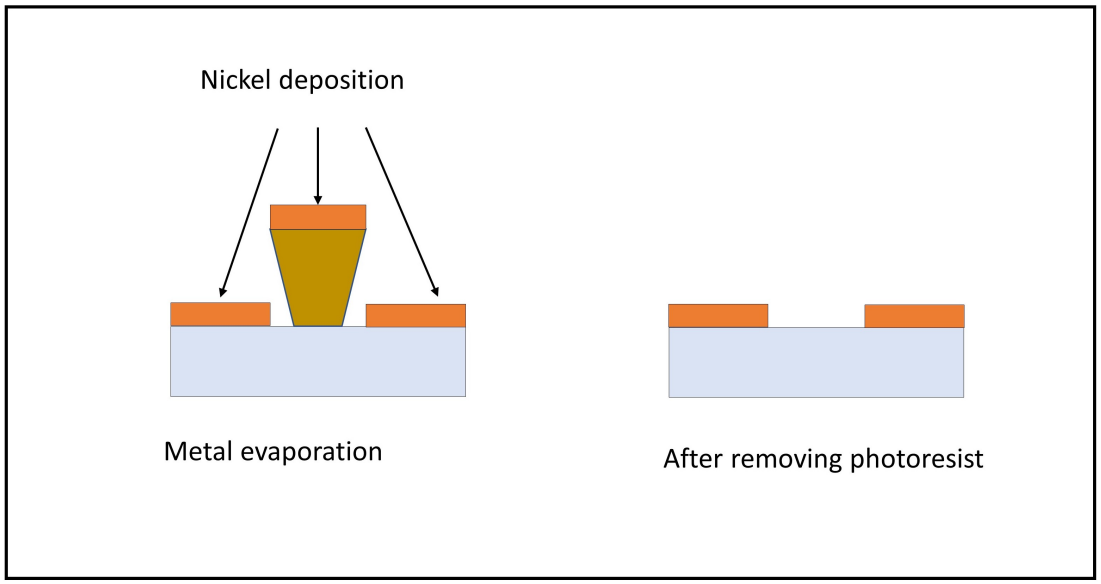

Figure 3.11: The profile of metal during the lift-off process.

3.1.7 Wire bonding and packaging

After metallization, the wafer is cleaved to get individual devices. We have used Silicon carbide scriber to cleave the wafer in the weak planes. We have used Indium (1.2x10-7 S/m) as a contact metal to connect the chip to the circuit. The

melting point of Indium metal is about 150°C. We have used soldering to melt down the indium and have made contact between the electrode pad and copper wire. A microfluidic channel is formed by placing a 1mm thick PDMS (Polydimethylsiloxane) film on the channel side of the chip. The chip is then mounted on an acrylic holder and the wires are connected to the header pins of the holder (Fig. 3.12). We have used two syringe caps to make the inlet and outlet (Fig. 3.12).

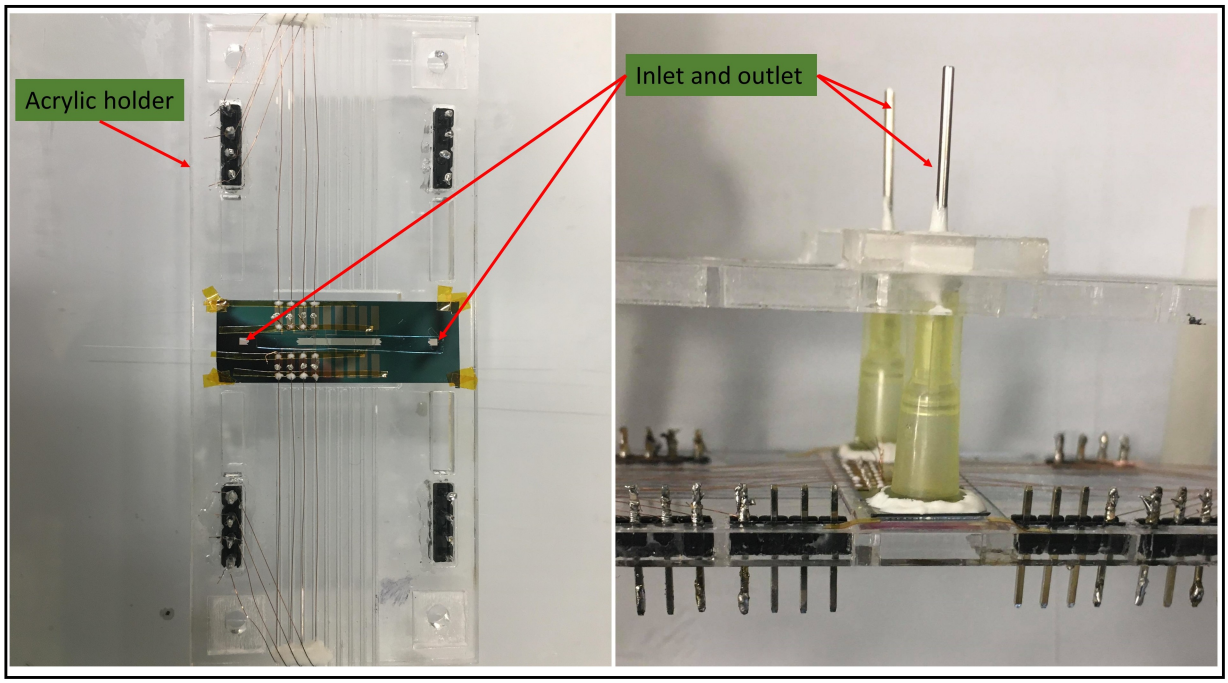

Figure 3.12: Device on an acrylic holder and inlet/outlet connections.

3.2 Device parameters

In this section, parameters of the device and device holder are given. Fig. 3.13 shows the top, side, and cross-sectional views of the device. We made an acrylic plate to hold the device. Fig. 3.14 shows a top and bottom view of the

device on the holder.

Length of the device: 30 mm

Width of the device: 10 mm

Thickness of Si: 300 μm

Thickness of SiO2: 0.25 μm

Thickness of the membrane (SiN): 0.5 μm

Thickness of RTD: 25 nm

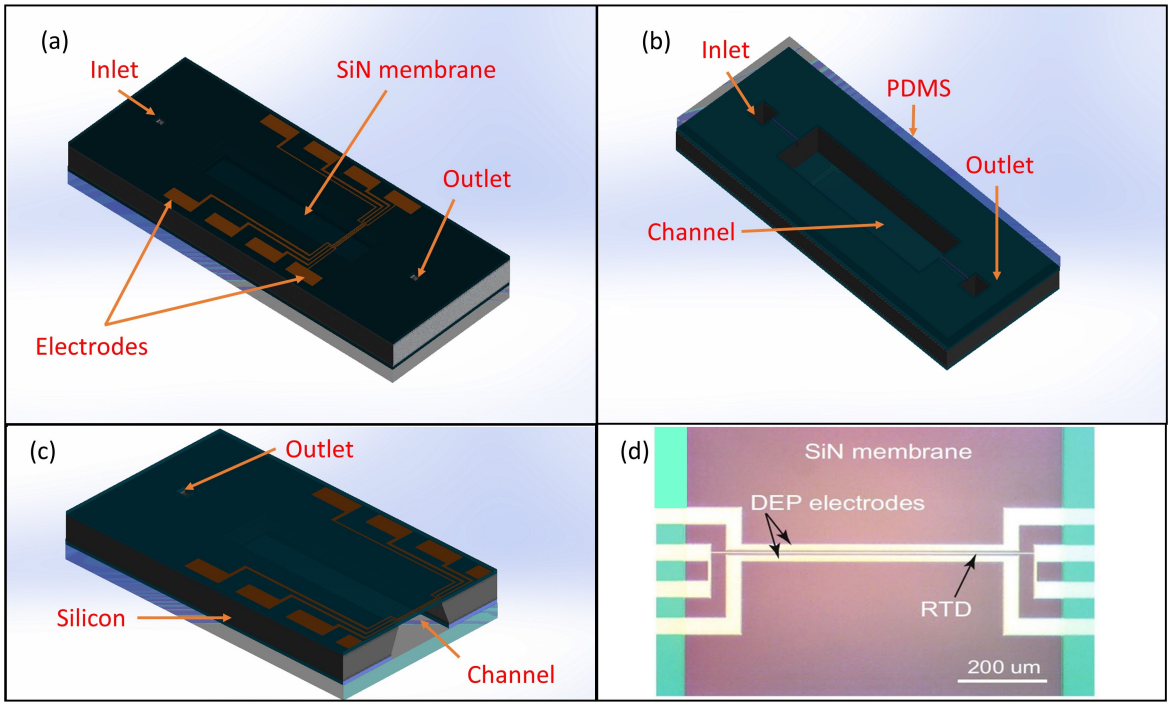

Figure 3.13: Device overview a) top view b) bottom view c) cross sectional view showing channel of the device d) close up optical photography.

Length of RTD: 720 μm

Width of RTD: 4 μm

Width of IDE: 20 μm

Distance between two IDEs: 10 μm

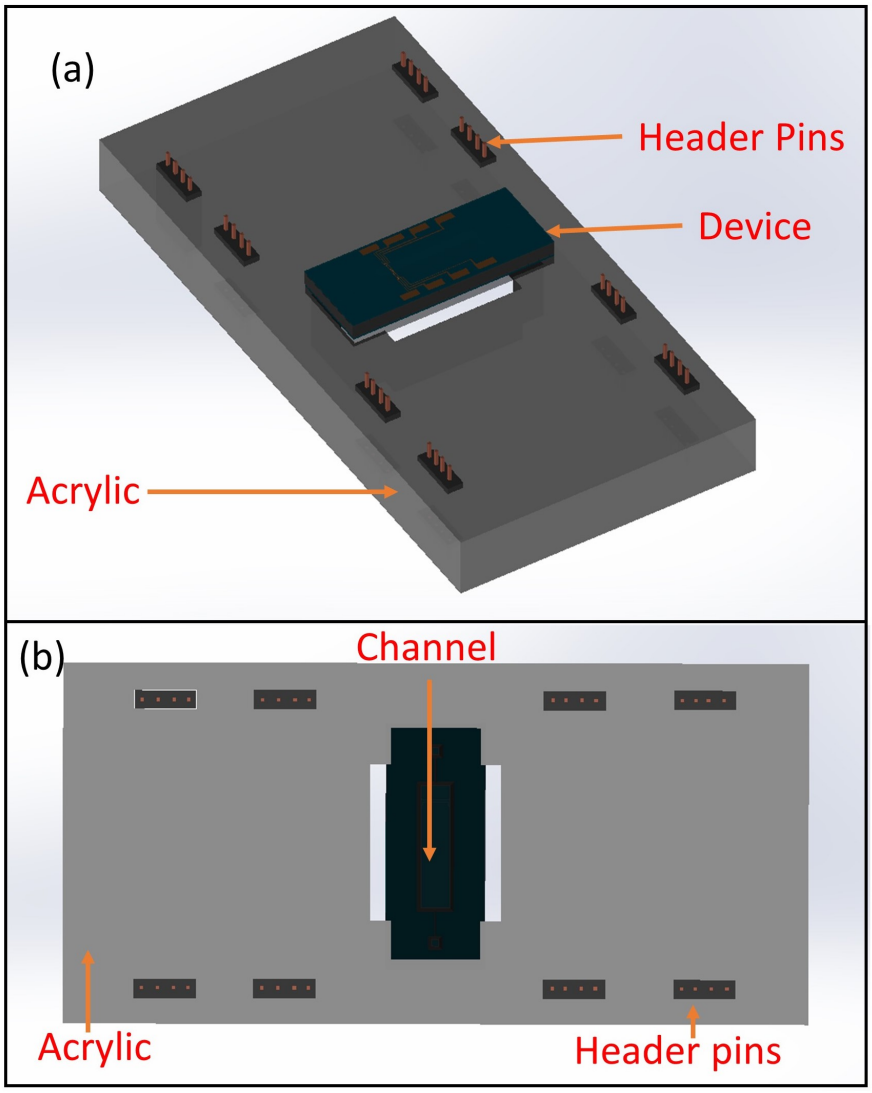

Figure 3.14: Device on top of an acrylic holder a) top view b) bottom view.

Distance between RTD and IDE: 3 μm

Width of electrode pad: 1 mm

Length of the electrode pad: 3 mm

Separation between two electrode pads: 0.5 mm

Thickness of acrylic plate: 3 mm

Width of acrylic plate: 35 mm

Length of acrylic plate: 80 mm

3.3 Experimental setup

We need two setups: one is to measure temperature coefficient (α), and another is for measuring temperature that is produced in DEP operation.

3.3.1 α measurement

The measurement of α is necessary to measure the temperature as a function of resistance. Our temperature sensor is connected to a Keithley 2400 in the four-wire configuration. A commercial RTD sensor (pt-100) is mounted near our device to measure the actual temperature. The excitation current of four-wire measurement for RTD is 0.1 mA, and for pt-100 is 1 mA. We have placed the device and RTD sensor in the top chamber of the flask. A double-wall, double-chambered, vacuum insulated thermal flask is used to measure α. The bottom chamber of the flask is filled with $50^{\circ}C$ hot water. We have used LabView software to collect data. Fig. 3.15 shows a schematic diagram of the α measurement setup.

In this experiment, we measure the temperature with pt-100 and resistance of our RTD sensor in 1 minute intervals. As water in the flask gradually cools down, the RTD sensor measures the resistance at the different temperatures inside the flask.

3.3.2 Temperature measurement

The device is placed on the stage of a microscope to visualize the cell capturing. Two IDEs of the DEP device are connected to the output of a 50x amplifier (TREK 2100HF), and a function generator (Keysight 33220 A) supplies the AC voltage to the amplifier. The output of the amplifier is monitored with an

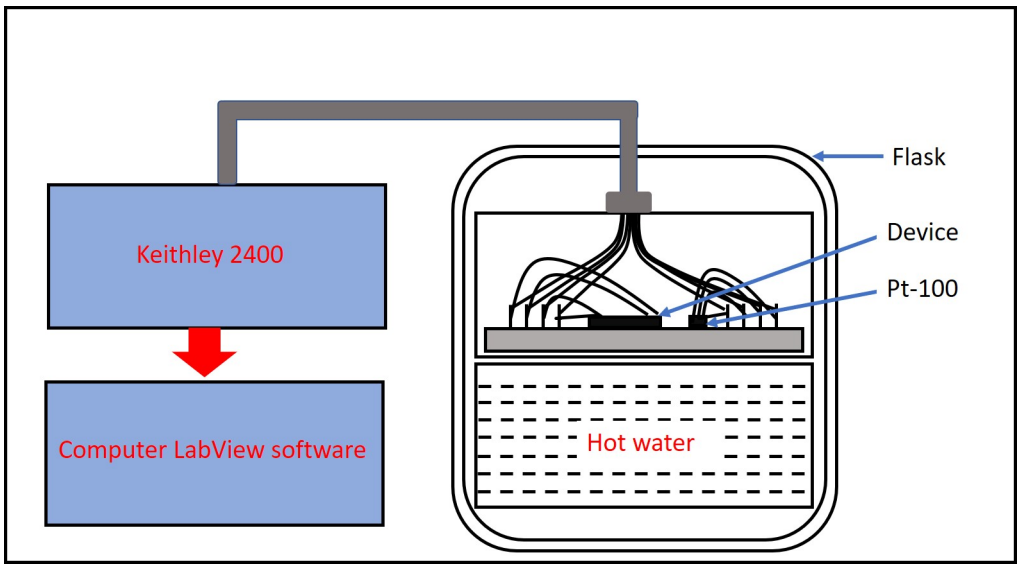

Figure 3.15: A schematic diagram of the (α) measurement setup.

oscilloscope (Keysight DSOX2004A). The temperature sensor is connected to a Keithley 2400 source/meter unit in a four-wire configuration. LabView software is used for controlling all these instruments and for data acquisition. Two reservoirs are used as solution source and drain. Fig. 3.16 shows the instrumental setup for measuring the temperature of the DEP device.

The DEP excitation and temperature measurement are set as follows. We have applied 5 V_{p-p} at 100 KHz frequency in DEP electrodes for 1.5 sec. Then the voltage is turned off. After around 100 ms, the RTD sensor measures the temperature. The DEP excitation and RTD measurement are performed sequentially to avoid coupling and interference between them. This DEP excitation and temperature measurement cycle are repeated for increasing voltage at the same frequency. The voltage increment is 5 V_{p-p}. After repeating this cycle for 6 trials, the final voltage has become 35 V_{p-p}. In the next cycle, the applied frequency is increased to 200 KHz, and the measurement is repeated for the same voltage range. The measurement continues up to 2 MHz with 100 KHz

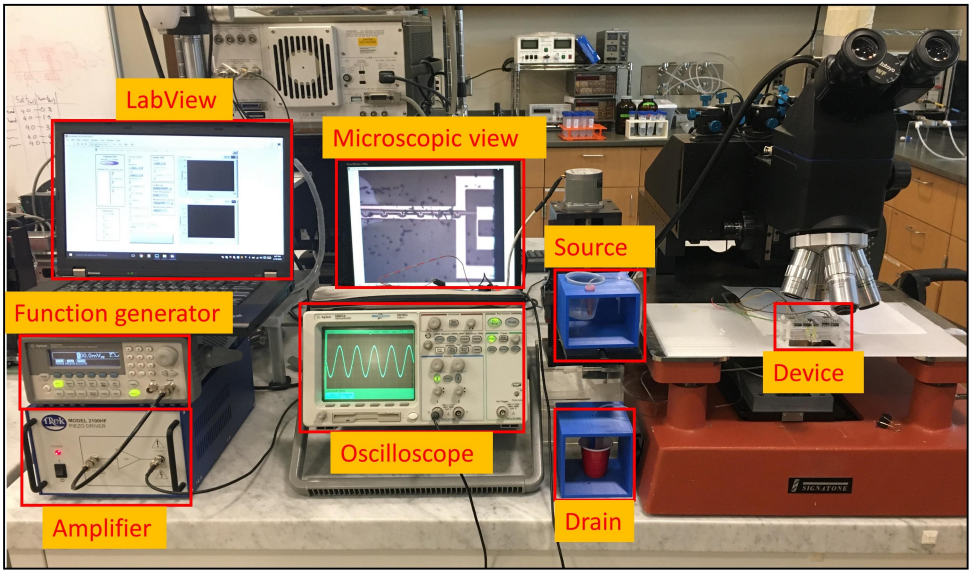

Figure 3.16: Instrumental setup of the DEP heat measurement.

increments. The channel is inspected by a microscope during the measurement process.

CHAPTER 4

RESULT AND DISCUSSION

4.1 Temperature coefficient measurement

Determining the value of the temperature coefficient (α) of an RTD sensor is very important for measuring accurate temperature. The resistance of the RTD sensor at different temperatures is measured. The experimental setup of the α measurement is described in Section 3.3.1. Fig. 4.1 shows the resistance of a 40nm thin Ni-RTD sensor at different temperatures. The temperature is measured by a pt-100 sensor. This experiment took place for 10 hours. The resistance and

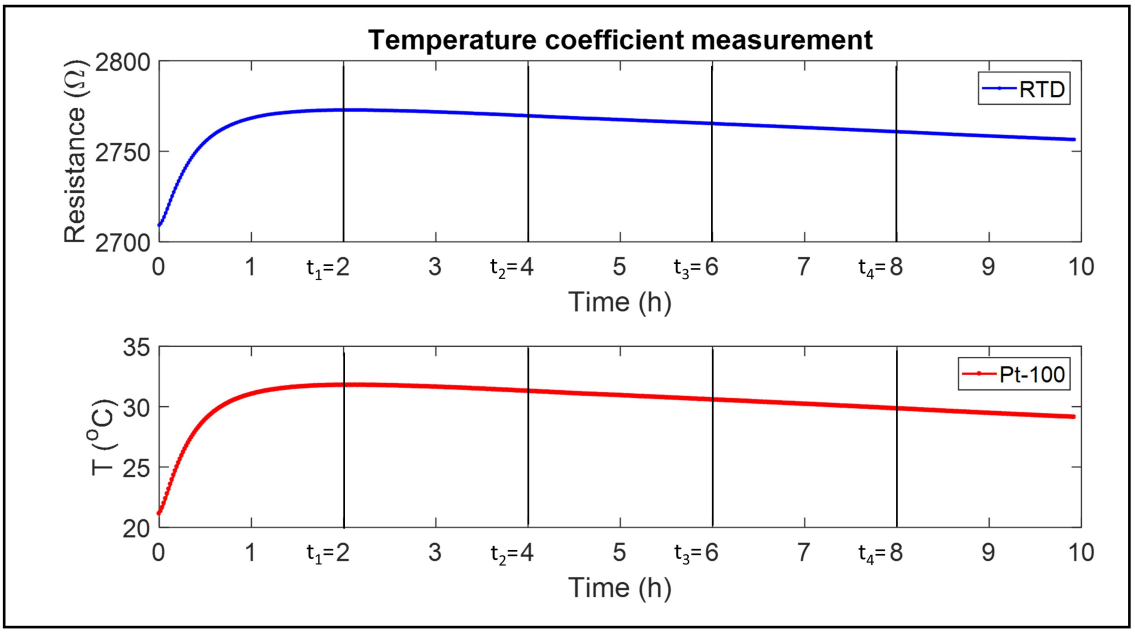

Figure 4.1: Resistance of a 40 nm thin Ni-RTD sensor at different temperature.

temperature are measured at 1-minute intervals. Four different times are chosen for measuring α. Table 4.1 shows different resistances and temperatures at

different times.

Time (hours)	Resistace of RTD (Ω)	Temperature ($^{\circ}C$)
t_1 =2	2772.780762	31.782264
t_2 =4	2769.620361	31.281939
t_3 =6	2765.365967	30.566256
t_4 =8	2760.822021	29.833095

Table 4.1: Resistance of a Ni-RTD sensor in different temperature.

The temperature coefficient is measured using Eq. 2.22. From four data points (t_1, t_2, t_3, t_4), we have measured three α values and then average them to get the most accurate α value. Table 4.2 shows the result of α measurement.

Data points	α
t_1, t_2	2.4559×10^{-3}
t_2, t_3	2.3008×10^{-3}
t_3, t_4	2.4060×10^{-3}
Average	2.3876×10^{-3}

Table 4.2: Temperature coefficient of Ni-RTD sensor.

4.2 Cell capture with DEP device

The functionality of the DEP device is tested by capturing yeast cells. The yeast cells are infused in the microfluidic channel of the DEP device. We have applied 1.5 MHz frequency, 15 V_{p-p} amplitude. The movement of cells is captured by a microscope. Fig. 4.2 shows the basic functionality of our device for handling yeast. The magnitude of the electric field in the device is stronger as it is closer to the edge of the IDE electrode and weaker as it is farther from the edge of

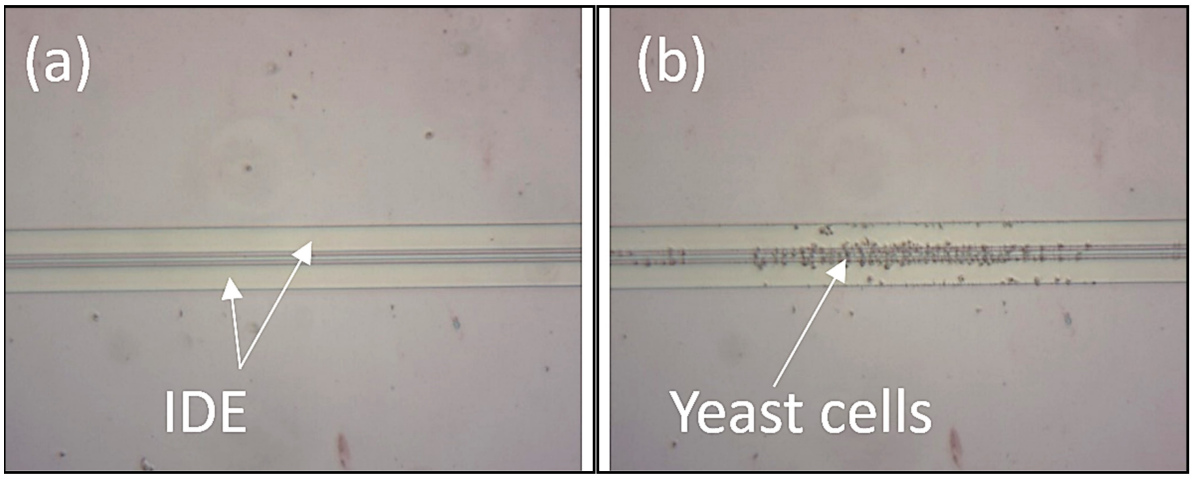

Figure 4.2: DEP operation on yeast cells. (a) before DEP, and (b) during DEP.

the IDE electrode. Therefore, particles affected by positive DEP will be pulled around the electrode edge, while particles affected by negative DEP will be pushed away from the IDE. Fig. 4.2 indicates the capability of particle manipulation under the positive DEP condition.

4.3 Detection of the heat in DEP device

The heat produced in DEP operation is observed optically. For optical detection, we have used a thermal imaging camera (FLIR E4). We have applied different frequencies of AC voltage in the DEP electrodes. At frequencies more than 200 kHz the heat can be clearly observed. As the frequency of applied voltage is increased, the intensity of heat is also increased. Fig. 4.3 shows the thermal image of the DEP device during DEP operation at 2 MHz frequency and 15 V_{p-p}. The heating was visualized instantly after applying the AC voltage and it disappeared instantly when turning off the output of the function generator.

Another experiment is done to make sure that what we observed is not a result of an artifact. we have fabricated a new device where two serpentine shape

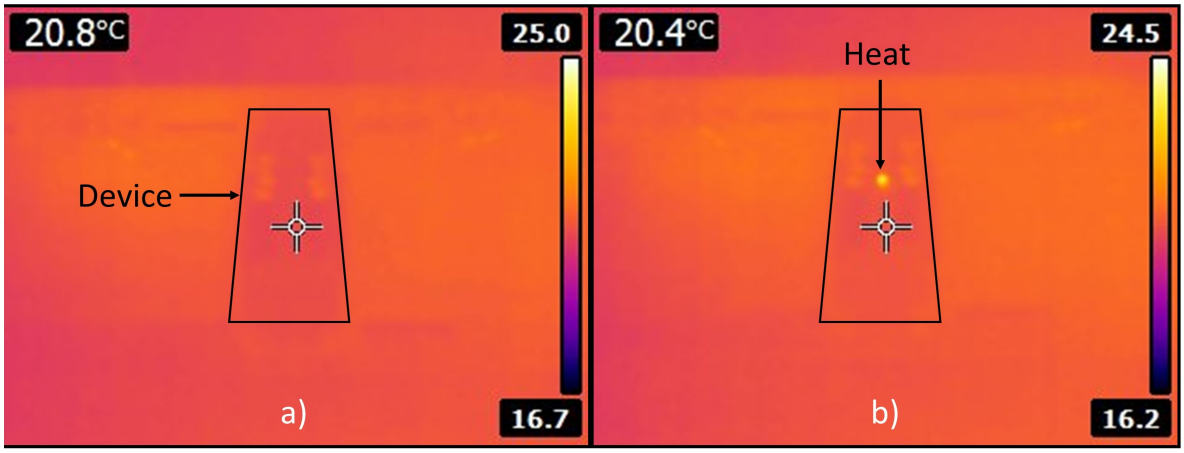

Figure 4.3: Thermal image (a) before DEP, and (b) during DEP.

RTD sensors are integrated, one is 1.4 mm away and another is 7.4 mm away from the DEP electrode. In this experiment, DI water flows from inlet to outlet through a microfluidic channel. If water is heated up during DEP operation, two RTD sensors can sense the heat as water will carry the heat from the DEP region to RTD sensors. Fig. 4.4 shows a schematic diagram of this device. We have created three different flow rates of DI water. We have started measuring the resistance near RTD (near to DEP) and Far RTD (far to DEP) and after 5 sec, 2 MHz 5 Vp-p voltage is applied in DEP electrodes with a function generator for 0.1 sec. The interval of resistance measurement is 38 ms.

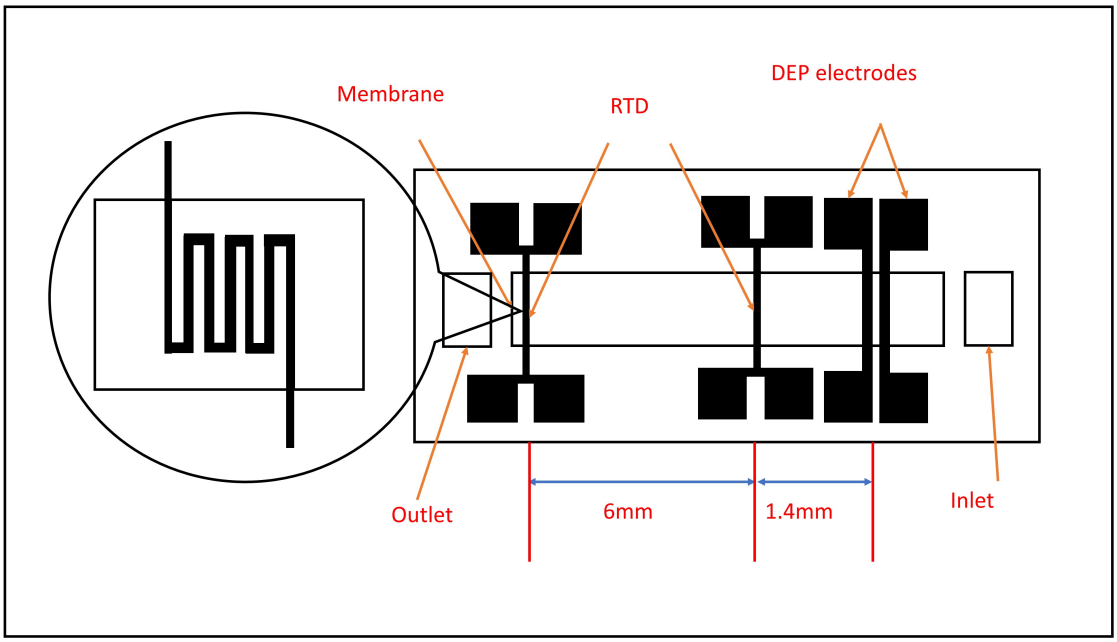

Figure 4.4: A schematic diagram of a DEP device with two RTD sensors.

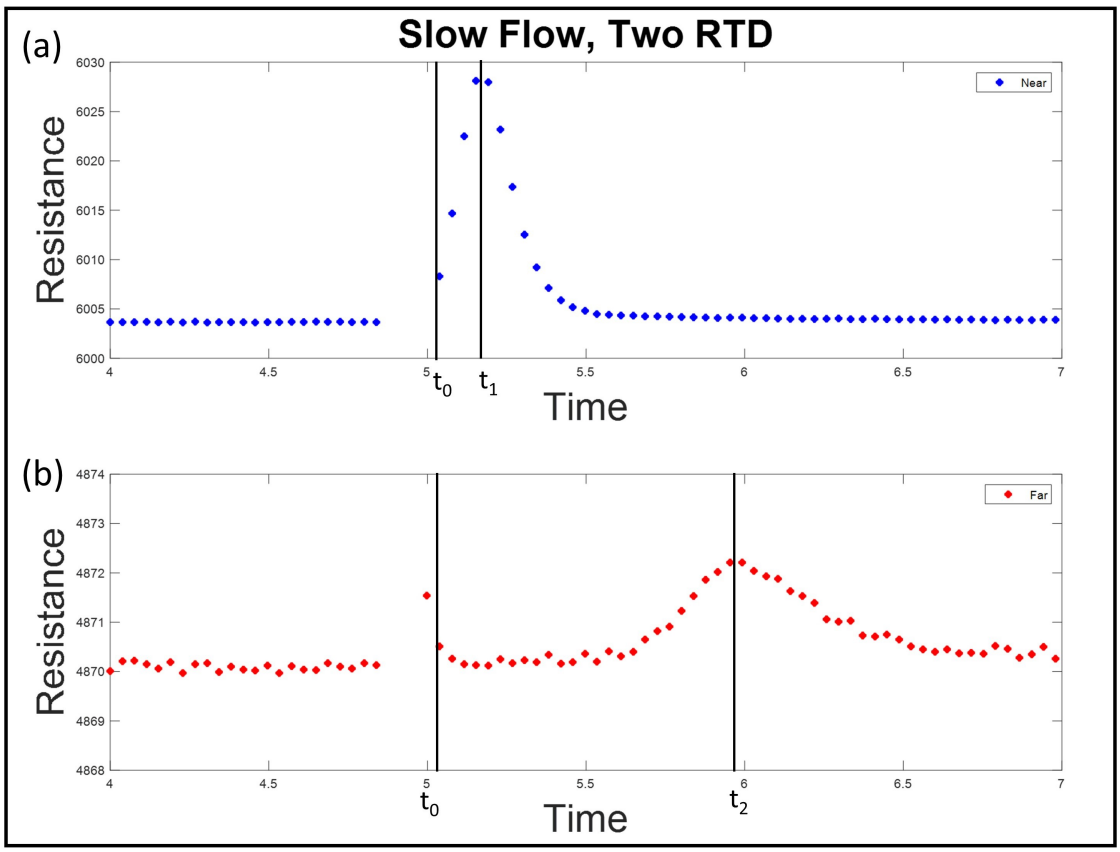

Figure 4.5: The response of RTD sensors, a) near RTD b) far RTD for slow flowrate of DI water.

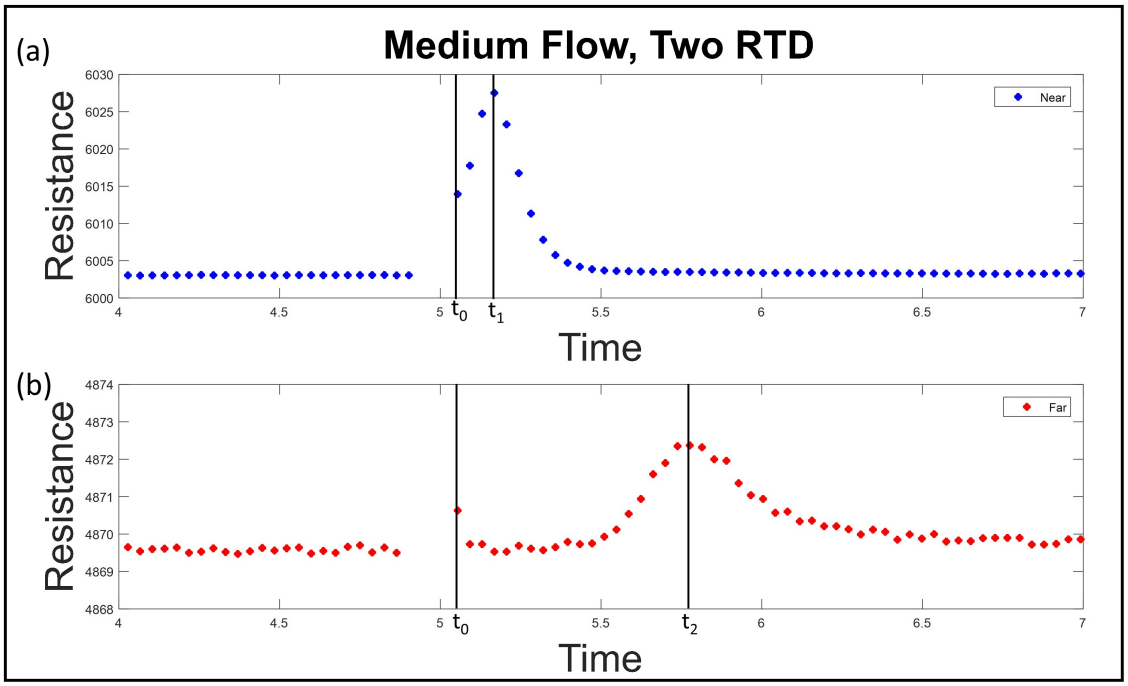

Figure 4.6: The response of RTD sensors, a) near RTD b) far RTD for medium flowrate of DI water.

Fig. 4.5, Fig. 4.6 and Fig. 4.7 show the response of two RTD sensors for slow, medium and fast flow of DI water. In these figures, t_0 indicates the time when the function generator is turned off. The peak resistance of near RTD is indicated at t_1 time and for far RTD at t_2 time. The distance between the two RTD is 6mm. The velocity of DI water is measured as:

$$V = \frac{6mm}{(t_2 - t_1)s} \tag{4.1}$$

Table 4.3 shows the measurement of velocity for different DI flows. The velocities of slow, medium and high flows are meaningful. This indicates the heat is transferred by DI water from the DEP device to RTD sensors. For further support, we have measured the heat detection time in near and far RTD sensors with the measured velocities. The time required for heat to be detected on near and far

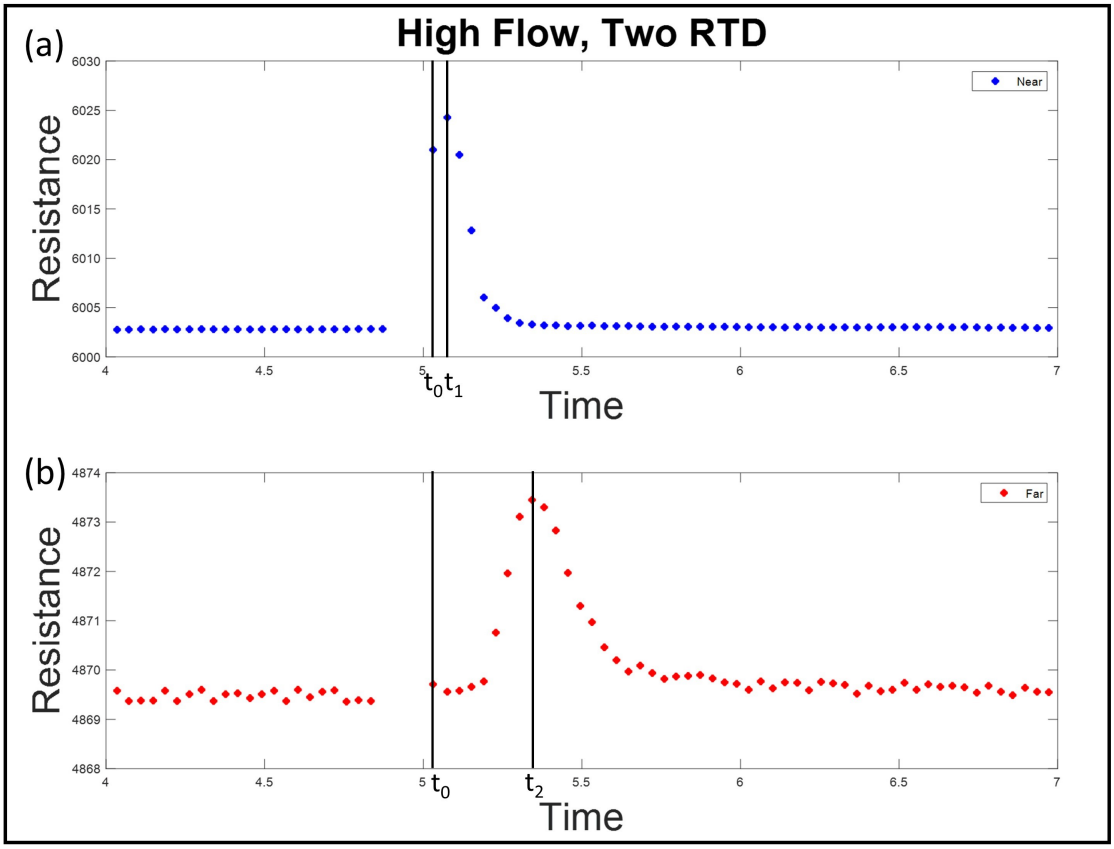

Figure 4.7: The response of RTD sensors, a) near RTD b) far RTD for high flowrate of DI water.

Flow type	Time t_1-t_0 (s), near RTD	Time t_2-t_0 (s), far RTD	Time difference, t_1-t_2 (s)	V (mm/s)
High	0.109	0.376	0.267	22.47
Medium	0.207	0.778	0.571	10.51
Slow	0.1869	1.002	0.8151	7.36

Table 4.3: Measurement of velocity for different DI flow.

RTD can be calculated by using the formula:

$$Time = \frac{distance}{velocity} \tag{4.2}$$

The calculated time and the measured time are presented in Table 4.4. In this experiment, we have detected heat in terms of resistance in two RTD sensors. The shape of resistance change is similar to the heat profile. Time (t_1-t_0) and (t_2-t_0) are considered as the heat detection time for near and far RTD. The calculated heat detection time and experimental time are in agreement with some errors. The error occurs in the time of near RTD for high and medium flows because we have applied heat for 100ms. In this time, heat already passed the near RTD sensor when the flow rate is high.

Flow type	Time (s), near RTD time		Time (s), far RTD	
	From data file t_0-t_1 (s)	Calculated time using velocity (s)	From data file t_0-t_2 (s)	Calculated time using velocity (s)
High	0.109	0.0623	0.376	0.329
Medium	0.207	0.133	0.778	0.704
Slow	0.1869	0.19	1.002	1.005

Table 4.4: Heat detection time in near and far RTD sensors.

4.4 Measurement of temperature in DEP device

We have measured the temperature in the DEP device with three different fluid samples (DI water, PBS, and 4% salt water) in the microfluidic channel. In Section 3.3.2, the details of this experiment are described. Fig 4.8, Fig 4.9, and Fig 4.10 show the temperature in DEP device when the channel is filled with DI water, PBS and 4% salt water respectively. Voltages are applied to IDEs for 1.5 s, and then the RTD measures the temperature for 1.5 s. The measurement cycle is repeated for the frequency range from 100 kHz to 2 MHz at frequency increments of 100 kHz. In Fig 4.8.c, Fig 4.9.c and, Fig 4.10.c, the temperature data is fitted with $T = Ae^{-t/\tau_{th}} + B$, which is the temperature cooling equation of a first-order

system.

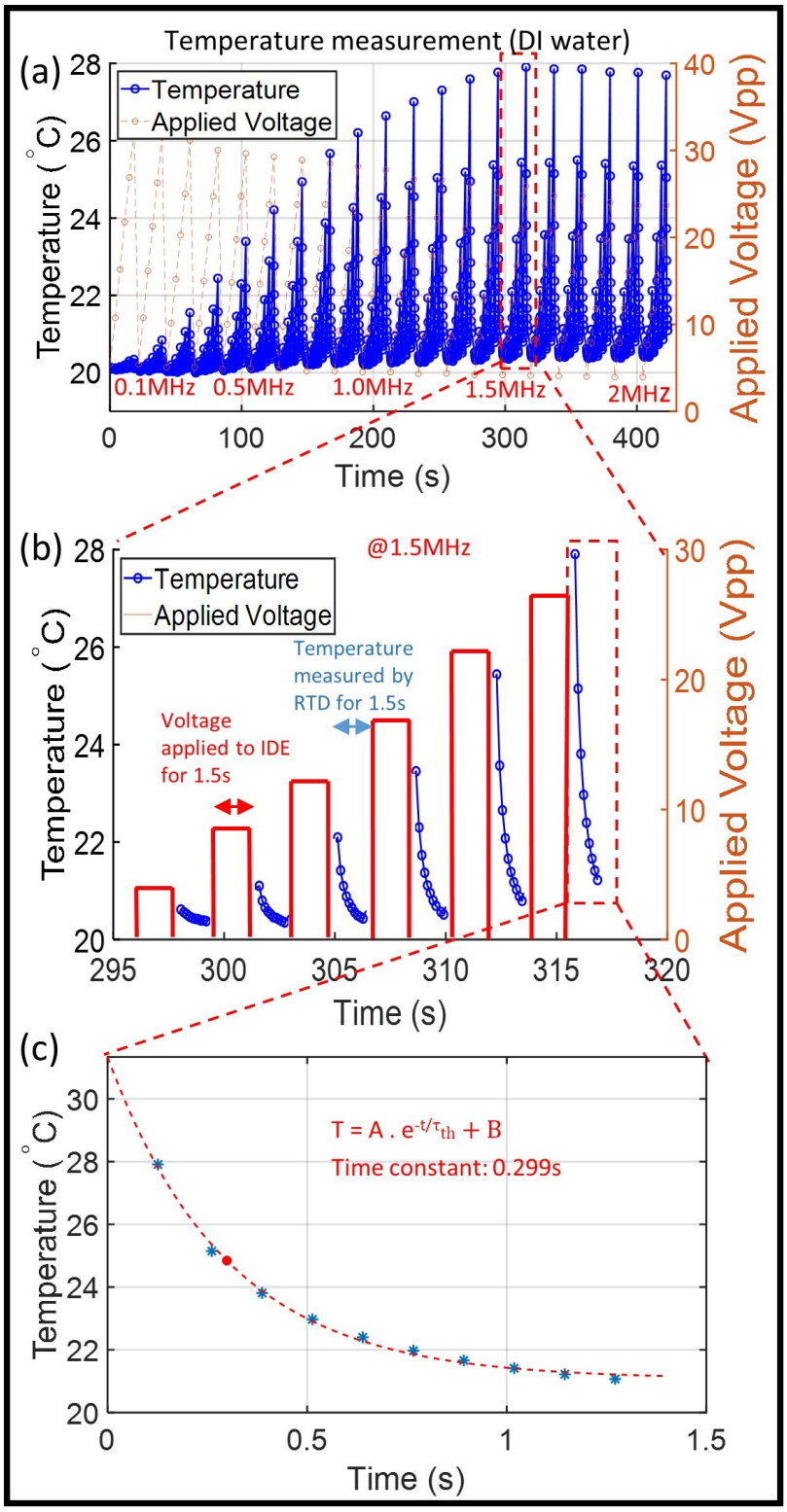

Figure 4.8: Measured temperature data as a function of time. The channel is filled with DI water. (a) Measured temperature data. (b) Close-up view of the dotted box in (a). (c) Close-up view of the dotted box in (b). The thermal time constant, τ_{th}, is 0.299 s when the channel is filled with DI water.

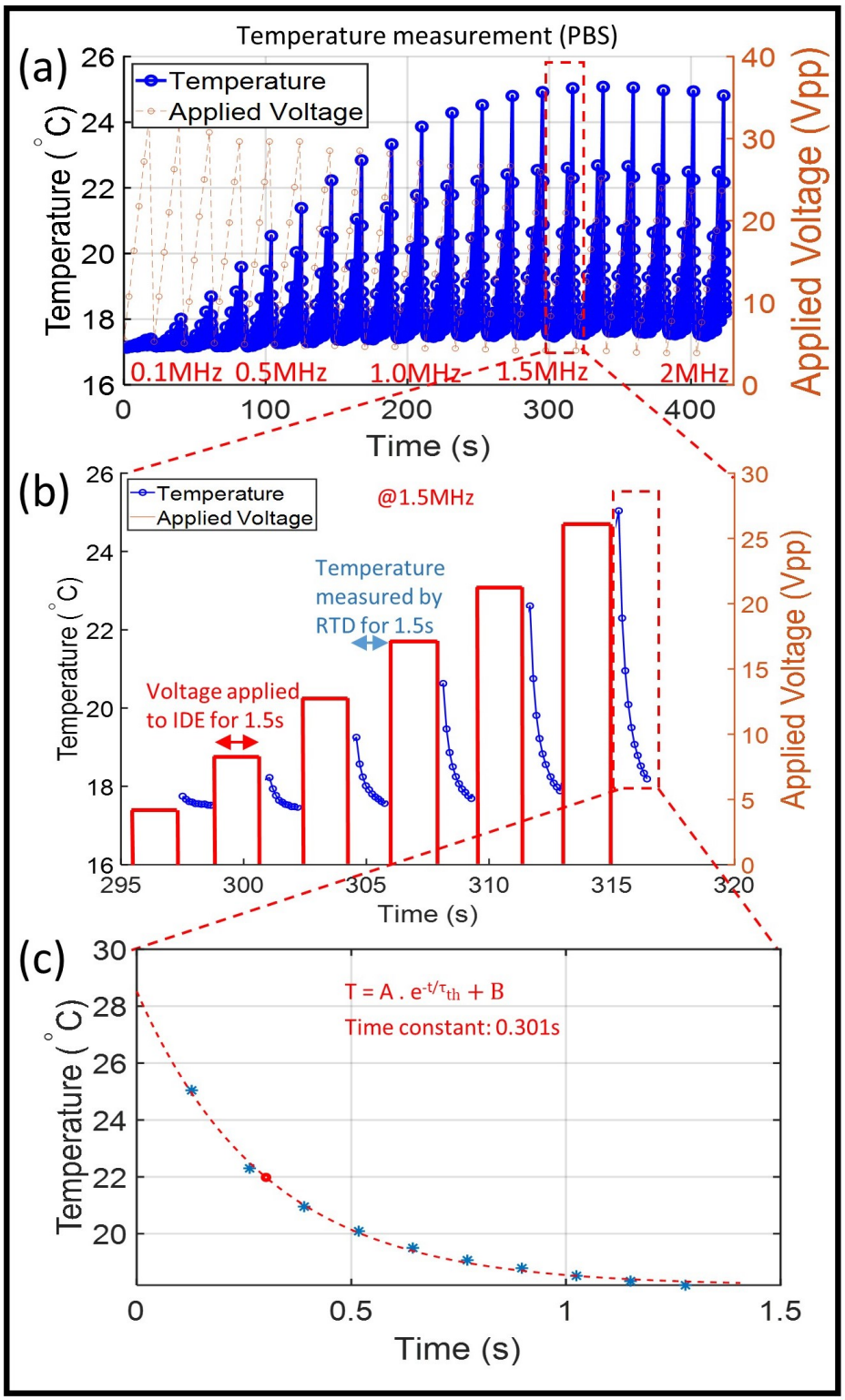

Figure 4.9: Measured temperature data as a function of time. The channel is filled with PBS. (a) Measured temperature data. (b) Close-up view of the dotted box in (a). (c) Close-up view of the dotted box in (b). The thermal time constant, τ_{th}, is 0.301 s when the channel is filled with PBS.

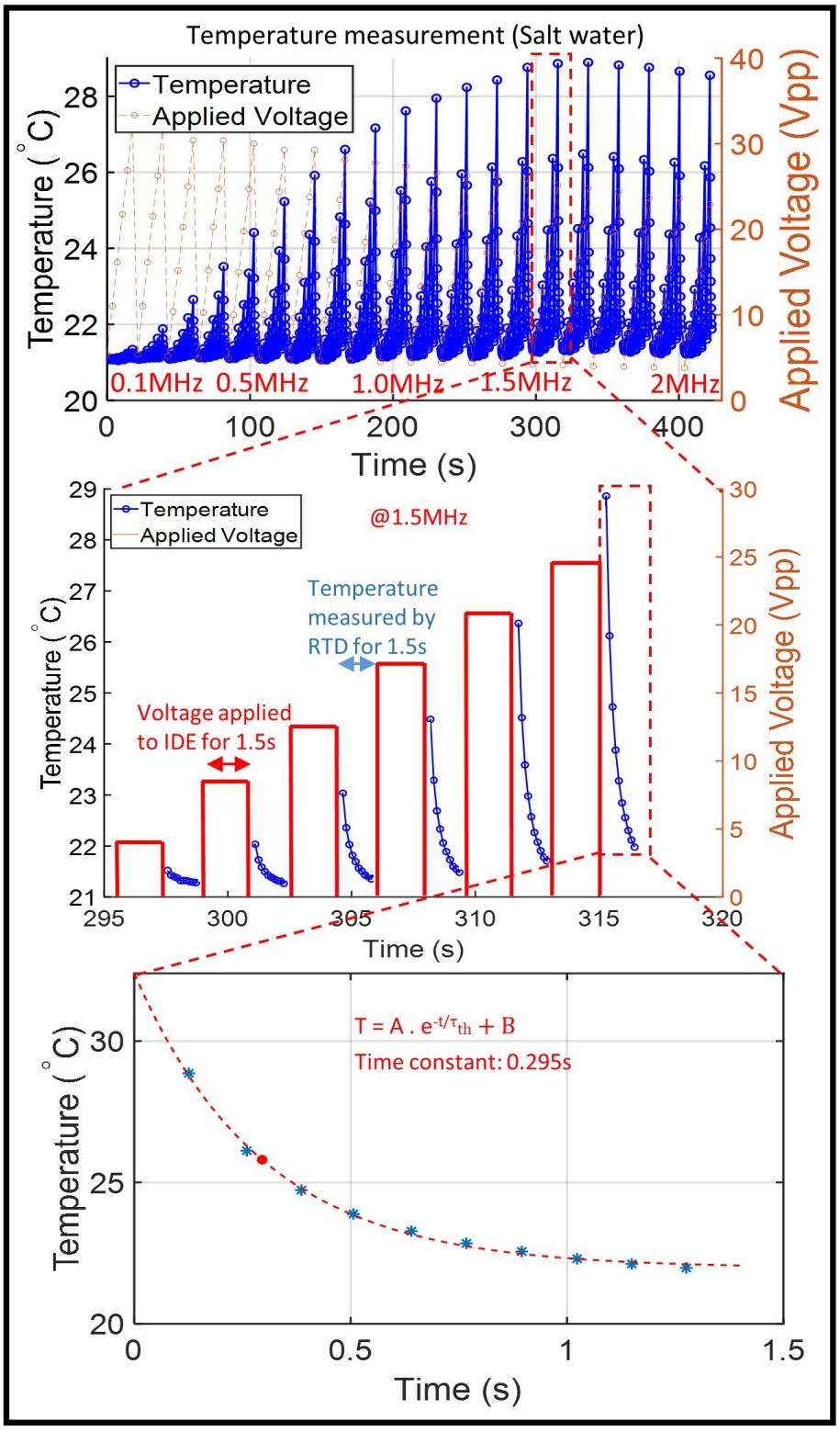

Figure 4.10: Measured temperature data as a function of time. The channel is filled with Salt (NaCl) water (4%). (a) Measured temperature data. (b) Close-up view of the dotted box in (a). (c) Close-up view of the dotted box in (b). The thermal time constant, τ_{th}, is 0.295 s when the channel is filled with Salt (NaCl) water (4%).

As shown in Fig 4.8.a, Fig 4.9.a, and Fig 4.10.a, the applied voltages at each frequency decrease due to the loading effect of the capacitive load (DEP). Therefore, the data is re-plotted as the maximum temperature increase divided by the applied voltage squared (ΔT per input power) as a function of the excitation frequency as shown in Fig 4.11. The ΔT is defined as $T_{measured}$ - $T_{abmient}$. The ΔT per input power of three samples (DI water, salt (NaCl) water (4%), and PBS) are shown in Fig 4.11. The temperature increases per unit power for all three samples are independent of the ion concentration in the media. This is another strong indication that the heating mechanism is due to the dielectric loss. Fig 4.11 shows that some noises exist at high frequencies.

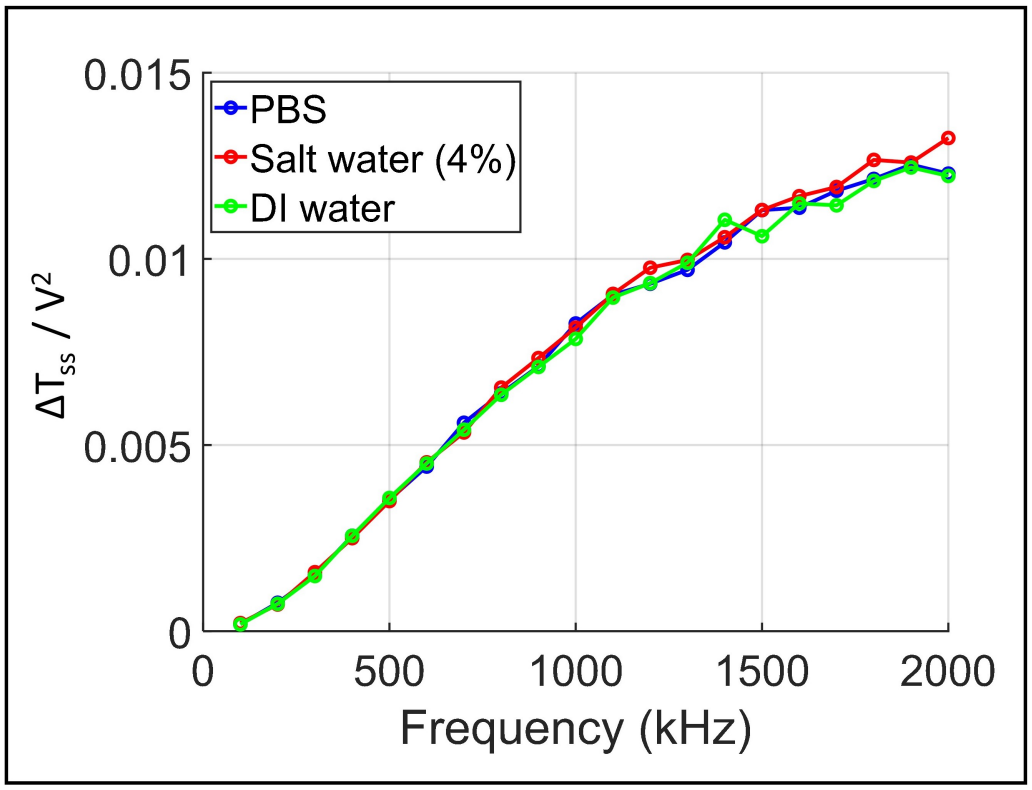

Figure 4.11: Measured ΔT per unit power (~V^2) of PBS, Salt (NaCl) water (4%), and DI water. No obvious difference between three samples is noticeable, indicating that no Joule heating mechanism is involved.

The heat generation in a dielectric material between electrodes can be analyzed with the Debye relaxation. Our DEP device is integrated on a SiN membrane. The SiN film is a good dielectric material (low electrical conductivity). The DEP device configuration can be modeled as a non-conventional capacitor consisting of exposed side-by-side plates with multiple dielectric materials (electrode-membrane-solution-membrane-electrode) in between. The apparent power flow into the capacitor is,

$$P_t = VI^* = -jV^2\omega C = -jV^2\frac{\omega A}{d}(\epsilon\,' - j\epsilon\,'') \tag{4.3}$$

where P_t is the total power delivered to the capacitor, V is the rms voltage applied, C is the capacitance of a lossy capacitor, ω is the applied angular frequency, A is the area of the capacitor, d is the distance between electrodes, $\epsilon\,'$ is the AC capacity (real part of the permittivity), and $\epsilon\,''$ is the dielectric loss factor (imaginary part of the permittivity). The heat generated by the Debye relaxation is described by the dielectric loss factor,

$$P_d = V^2\frac{\omega A}{d}\epsilon\,'' \tag{4.4}$$

where P_d is the power dissipated in the capacitor. From Eq. 2.30, dielectric loss factor can be written as,

$$P_d = V^2\frac{A}{d\tau_d}(\epsilon_\infty - \epsilon_0)\frac{(\omega\tau_d)^2}{1+\omega^2\tau_d^2} \tag{4.5}$$

where, ϵ_0 is the permittivity at frequencies below dipole relaxation, ϵ_∞ is the permittivity at frequencies above dipole relaxation, and τ_d is the Debye relaxation time constant.

The power, P_d, is dissipated in the capacitor. Since the power is applied for a given time to the capacitor, the step response of a first-order system can be used to obtain the temperature response using Fourier's Law of heat conduction which

is described in Section 2.4. The temperature increase or decrease in the capacitor by a step power input is,

$$\Delta T(t) = P_d R_t[1 - exp(-t/\tau_{th})] \tag{4.6}$$

$$\Delta T(t) = P_d R_t exp(-t/\tau_{th}) \tag{4.7}$$

where $\Delta T(t) = T_{cap(t)} - T_{amb}$, $T_{cap(t)}$ is the temperature of the capacitor, T_{amb} is the ambient temperature, R_t is the thermal resistance between the capacitor and ambient, and τ_{th} is the thermal time constant. The time constant, τ_{th}, can be measured directly as shown in Fig 4.8.c, Fig 4.9.c, Fig 4.10.c and has values of 0.299s, 0.301s and 0.295s with DI water, PBS and salt (NaCl) water (4%), respectively. The time period of the applied power to the capacitor is 1.5 second. Therefore, the temperature of the capacitor reaches the steady state temperature, ΔT_{ss}. The thermal time constant is obtained by fitting Eq. 4.7 with the data. From the dielectric loss and the first order thermal analysis, the steady state temperature increase from the ambient temperature of the capacitor can be expressed as,

$$\Delta T_{ss} = P_d R_t \tag{4.8}$$

Assuming all the dielectric loss is converted to heat, the steady state temperature can be written as,

$$\Delta T_{ss} = V^2 R_t \frac{A(\epsilon_\infty - \epsilon_0)}{d\tau_d} \frac{(\omega\tau_d)^2}{1 + \omega^2\tau_d^2} \tag{4.9}$$

$\Delta Tss/V^2$ as a function of frequency $(f = \omega/2\pi)$ is shown in Fig 4.12. The data is fitted with the dielectric power loss equation,

$$y = a\frac{(b.f)^2}{[1 + (b.f)^2]} \tag{4.10}$$

with a = 0.0152 and b = 1.1×10^6. a is $R_t A(\epsilon_0\epsilon_\infty)/d\tau_d$ in Eq. 4.9. b is the Debye time constant, τ_d, in seconds. The regression, R^2, is higher than 0.999, indicating

the analysis is in good agreement with the data. This work is published in the Scientific Report journal [48].

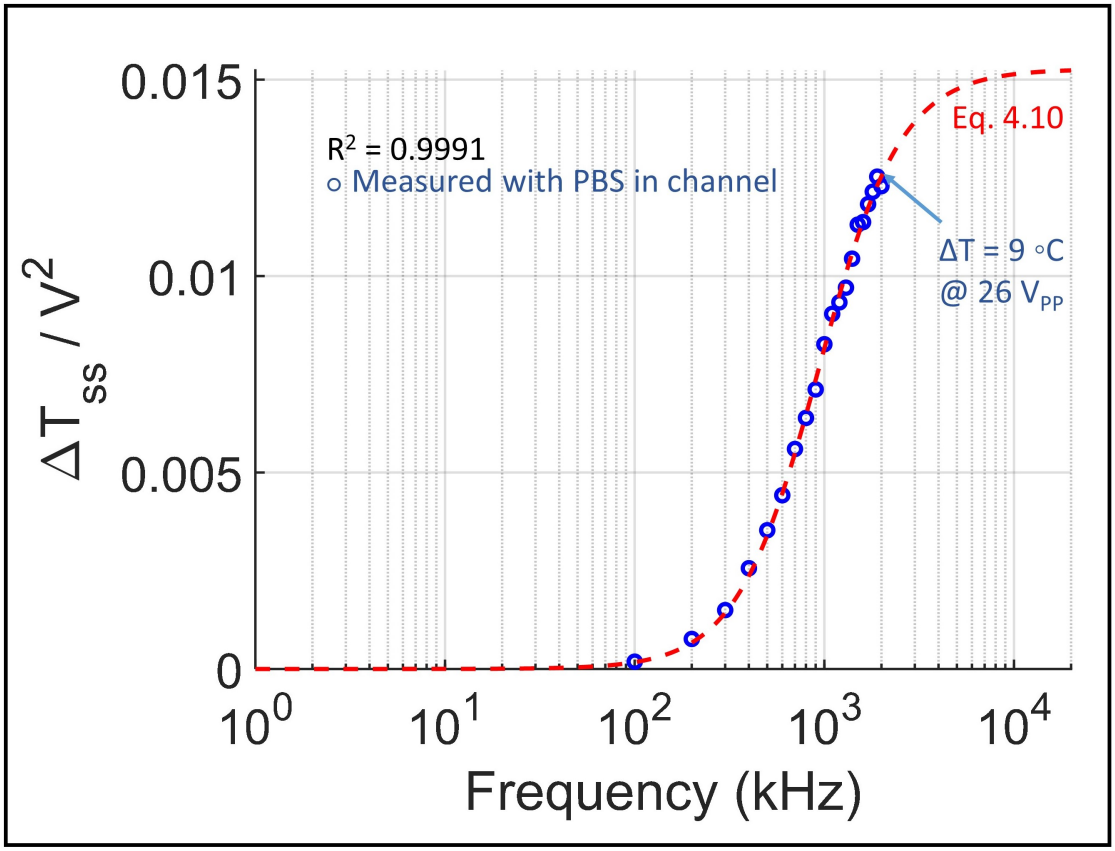

Figure 4.12: Temperature increase per applied voltage squared (unit power) due to the dielectric loss in a DEP device as a function of frequency. The maximum ΔT for PBS in the channel is 9 °C, at an applied voltage of 26 V_{pp}. The temperature is measured with PBS solution in the channel. The measured data is in good agreement with the dielectric loss analysis (Eq. 4.10). The blue circles are measured data. The red dotted line is the power dissipated in the capacitor (Eq. 4.10). The regression of the data fit is higher than 0.999.

CHAPTER 5

CONCLUSION AND FUTURE WORK

5.1 Conclusion

The approaches to avoid heating in the past studies using DEP have mainly tried to reduce Joule heating; however, we suggest that the dielectric characteristics of material have to be considered to reduce the dielectric loss and to reduce heat generation in microfluidic devices.

The resistance temperature detector based temperature measurement method and the Debye relaxation analysis find that significant heat is generated when an alternating voltage is applied to the electrically insulated interdigitated electrodes based dielectrophoretic device. The experimental results are in good agreement with the theoretical calculations.

The experimental results and analysis indicate that the origin of the heat generation in the DEP devices with electrically insulated electrodes is the Debye relaxation rather than Joule heating.

The heat generated from the Debye relaxation is highly localized between the IDEs and is more reliable than that from Joule heating, which can be used as a heating element for micro/nano-scale devices.

5.2 Future work

The localized dielectric heating process can be used as a powerful tool in a wide range of biological studies, because the heating can be easily controlled by the design, driving voltage/frequency, and materials used in the micro/nano-scale devices. The effect of temperature on cell growth rate has been studied for many years. Experimental work combining temperature effect and

life cycle analysis can be done by using localized dielectric heating where a limited number of cells are needed.

The most challenging problem we faced in this experiment is the presence of electromagnetic coupling when we tried to apply the DEP voltage and tried to measure temperature simultaneously. If it is possible to cancel out the electromagnetic coupling, we may able to measure the exact temperature without predicting the temperature from the fitting curve. In the cell capture applications, reducing dielectric heating will be a challenge for the future. One probable approach is to capture cells by applying a low-frequency signal on DEP electrodes as low-frequency voltage produces less heat in the DEP devices.

Currently, different flowmeters exist to measure the flow rate of a fluid. However, there are few technologies that can measure the flow rate avoiding direct contact with a fluid. The measurement of microflow rates is critical in several applications, such as semiconductor manufacturing processes, medical drug injection, and chemical processes. The most widely used microflow sensor is the thermal mass flow sensor. The dielectric heating may also be used as a source of heating in the thermal mass flow sensor.

BIBLIOGRAPHY

[1] D. Anderson, *Keys to achieving high accuracy and reliability in temperature measurement* (2014). Available at `https://www.controleng.com/articles/keys-to-achieving-high-accuracy-and-reliability-in-temperature-measurement/`.

[2] G.M. Hallegraeff, J.P. Valentine, J.A. Marshall, and C.J. Bolch, *Temperature tolerances of toxic dinoflagellate cysts: application to the treatment of ships' ballast water*, Aquatic Ecology 31 (1997), pp. 47–52.

[3] M.W. Dewhirst, J. Abraham, and B. Viglianti, *Evolution of thermal dosimetry for application of hyperthermia to treat cancer*, in *Advances in heat transfer*, Vol. 47, Elsevier, 2015, pp. 397–421.

[4] M. Suzuki, V. Zeeb, S. Arai, K. Oyama, and S. Ishiwata, *The 10 5 gap issue between calculation and measurement in single-cell thermometry*, Nature methods 12 (2015), p. 802.

[5] B. Baker, *Temperature sensing technologies*, AN679, Microchip Technology Inc (1998).

[6] J. Fraden, *Noncontact active temperature sensor* (1997). US Patent 5,645,349.

[7] C. Hagart-Alexander, *Temperature measurement*, in *Instrumentation reference book*, Elsevier, 2003, pp. 239–302.

[8] J.M. Kurt, *Thermometer* (1955). US Patent 2,723,564.

[9] W. Boyes, *Instrumentation Reference Book*, Elsevier, 2010.

[10] P.R. Childs, J. Greenwood, and C. Long, *Review of temperature measurement*, Review of scientific instruments 71 (2000), pp. 2959–2978.

[11] K. Lacanette, *Tutorial 4679: Thermal management handbook* (2014). Available at `www.maximintegrated.com/en/app-notes/index.mvp/id/4679`.

[12] J.S. Steinhart and S.R. Hart, *Calibration curves for thermistors*, in *Deep Sea Research and Oceanographic Abstracts*, Vol. 15. Elsevier, 1968, pp. 497–503.

[13] *The fundamentals of rtd temperature sensors* (2013). Available at `www.prelectronics.com/the-fundamentals-of-rtd-temperature-sensors/`.

[14] L. Sander, *Fiber optical temperature sensors* (1981). US Patent 4,278,349.

[15] K. Kyuma, S. Tai, T. Sawada, and M. Nunoshita, *Fiber-optic instrument for temperature measurement*, IEEE Transactions on Microwave Theory and Techniques 30 (1982), pp. 522–525.

[16] *Thermal imaging guidebook for building and renewable energy applications* (2011). Available at `http://www.flir.com`.

[17] P.R. Gascoyne, X.B. Wang, Y. Huang, and F.F. Becker, *Dielectrophoretic separation of cancer cells from blood*, IEEE transactions on industry applications 33 (1997), pp. 670–678.

[18] H. Morgan, M.P. Hughes, and N.G. Green, *Separation of submicron bioparticles by dielectrophoresis*, Biophysical journal 77 (1999), pp. 516–525.

[19] L.C. Hsiung, C.L. Chiang, C.H. Wang, Y.H. Huang, C.T. Kuo, J.Y. Cheng, C.H. Lin, V. Wu, H.Y. Chou, D.S. Jong, *et al.*, *Dielectrophoresis-based cellular microarray chip for anticancer drug screening in perfusion microenvironments*, Lab on a Chip 11 (2011), pp. 2333–2342.

[20] Y. Nakashima, S. Hata, and T. Yasuda, *Blood plasma separation and extraction from a minute amount of blood using dielectrophoretic and capillary forces*, Sensors and Actuators B: Chemical 145 (2010), pp. 561–569.

[21] E.D. Pratt, C. Huang, B.G. Hawkins, J.P. Gleghorn, and B.J. Kirby, *Rare cell capture in microfluidic devices*, Chemical engineering science 66 (2011), pp. 1508–1522.

[22] N. Abd Rahman, F. Ibrahim, and B. Yafouz, *Dielectrophoresis for biomedical sciences applications: A review*, Sensors 17 (2017), p. 449.

[23] H.A. Pohl, *Dielectrophoresis: The behavior of neutral matter in nonuniform electric fields (Cambridge Monographs on physics)*, Cambridge/New York: Cambridge University Press, 1978.

[24] G.H. Markx, P.A. Dyda, and R. Pethig, *Dielectrophoretic separation of bacteria using a conductivity gradient*, Journal of biotechnology 51 (1996), pp. 175–180.

[25] C. Rosa, E. Capelas de Oliveira, *et al.*, *Relaxation equations: fractional models*, Journal of Physical Mathematics 6 (2015).

[26] M.P. Hughes, *Fifty years of dielectrophoretic cell separation technology*, Biomicrofluidics 10 (2016), p. 032801.

[27] U. Seger-Sauli, M. Panayiotou, S. Schnydrig, M. Jordan, and P. Renaud, *Temperature measurements in microfluidic systems: Heat dissipation of negative dielectrophoresis barriers*, Electrophoresis 26 (2005), pp. 2239–2246.

[28] H. Glasser, T. Schnelle, T. Müller, and G. Fuhr, *Electric field calibration in micro-electrode chambers by temperature measurements*, Thermochimica acta 333 (1999), pp. 183–190.

[29] R.C. Gallo-Villanueva, V.H. Perez-Gonzalez, B. Cardenas-Benitez, B. Jind, S.O. Martinez-Chapa, and B.H. Lapizco-Encinas, *Joule heating effects in optimized insulator-based dielectrophoretic devices: An interplay between post geometry and temperature rise*, Electrophoresis 40 (2019), pp. 1408–1416.

[30] K. Okabe, N. Inada, C. Gota, Y. Harada, T. Funatsu, and S. Uchiyama, *Intracellular temperature mapping with a fluorescent polymeric thermometer and fluorescence lifetime imaging microscopy*, Nature communications 3 (2012), pp. 1–9.

[31] S. Higaki, B.M. Gebhardt, W.J. Lukiw, H.W. Thompson, and J.M. Hill, *Gene expression profiling in the hsv-1 latently infected mouse trigeminal ganglia following hyperthermic stress*, Current eye research 26 (2003), pp. 231–238.

[32] C. Qian, H. Huang, L. Chen, X. Li, Z. Ge, T. Chen, Z. Yang, and L. Sun, *Dielectrophoresis for bioparticle manipulation*, International journal of molecular sciences 15 (2014), pp. 18281–18309.

[33] J.D. et al., *Energy education - thermal energy* (2017). Available at `https://energyeducation.ca/encyclopedia/Thermal_energy`.

[34] J.D. et al., *Energy education - temperature* (2017). Available at `https://energyeducation.ca/encyclopedia/Heat`.

[35] M. Ghassemi and A. Shahidian, *Nano and bio heat transfer and fluid flow*, Academic Press, 2017.

[36] H. Zhang, *Building materials in civil engineering*, Elsevier, 2011.

[37] J.H. Lienhard, *A heat transfer textbook*, Courier Dover Publications, 2019.

[38] Bahrami, *Transient heat conduction* (2015). Available at `https://fliphtml5.com/cumy/suue/basic`.

[39] A.M. Helmenstine, *Table of electrical resistivity and conductivity* (2019). Available at `https://www.thoughtco.com/`

table-of-electrical-resistivity-conductivity-608499.

[40] T.R. Kuphaldt, *Temperature coefficient of resistance*. Available at https://www.allaboutcircuits.com/textbook/direct-current/chpt-12/temperature-coefficient-resistance/.

[41] K.C. Kao, *Dielectric phenomena in solids*, Elsevier, 2004.

[42] M.J. Madou, *Fundamentals of microfabrication: the science of miniaturization*, CRC press, 2002.

[43] B. Davaji, H.D. Cho, M. Malakoutian, J.K. Lee, G. Panin, T.W. Kang, and C.H. Lee, *A patterned single layer graphene resistance temperature sensor*, Scientific reports 7 (2017), pp. 1–10.

[44] G. Sahni, *Micro electro mechanical systems (mems)* (2000).

[45] P. Stevic, *Boe/hf–silicon dioxide etching standard operating procedure* (2018). Available at https://d1rkab7tlqy5f1.cloudfront.net/TNW/Afdelingen/Quantum%20Nanoscience/Kavli%20Nanolab%20Delft/Equipment/BOE-HF%20SOP%20Silicon%20Etching.pdf.

[46] *Image reversal resists and their processing, micro chemicals*. Available at www.microchemicals.com/technical_information/image_reversal_resists.pdf.

[47] *Image reversal photoresists, micro chemicals*. Available at www.microchemicals.com/products/photoresists/image_reversallift_off.html.

[48] T.J. Kwak, I. Hossen, R. Bashir, W.J. Chang, and C.H. Lee, *Localized dielectric loss heating in dielectrophoresis devices*, Scientific Reports 9 (2019), pp. 1–9.